Ocean Engineering 227 (2021) 108841

Contents lists available at ScienceDirect

Ocean Engineering

journal homepage: www.elsevier.com/locate/oceaneng

A potential flow method combining immersed boundaries and overlapping grids: Formulation, validation and verification

Finn-Christian Wickmann Hanssen [a,*], Marilena Greco [a,b]

[a] Centre for Autonomous Marine Operations and Systems (NTNU AMOS), Department of Marine Technology, NTNU, Trondheim, Norway
[b] CNR-INM, Institute of Marine Engineering, Via di Vallerano 139, 00128 Roma, Italy

ARTICLE INFO

Keywords:
Nonlinear potential flow theory
Harmonic polynomial cell method
Numerical wave tank
Wave propagation
Wave–body interaction

ABSTRACT

A fully nonlinear two-dimensional numerical method based on potential-flow theory for water waves and their interaction with surface-piercing rigid bodies is presented. The harmonic polynomial cell (HPC) method is used to solve the Laplace equation for the velocity potential and its time derivative. The HPC method, which is a high-order method using analytical expressions (harmonic polynomials) to represent the solution inside overlapping cells, has previously been shown accurate and efficient. Supplementary research has shown that, in order to maximally benefit from the method's accuracy, it is a requirement that square or close-to-square cells are used. Here, we use an immersed boundary method to model non-stationary boundaries such as the free surface or the surface of a rigid body, and overlapping, body-fixed grids that are locally Cartesian to refine the solution near moving bodies. Combining these two modelling concepts with the HPC method represents the main novel contribution in the present work. With this combined method, denoted as an immersed-boundary overlapping grid method (IBOGM), the challenge of generating boundary-fitted grids for complex boundaries is avoided. Moreover, square cells can be used throughout the domain and the solution can be refined locally without increasing the number of unknowns unnecessarily. The method is systematically validated and verified against analytical, experimental and numerical reference results. The cases studied include propagation of steep waves, forced heave motions of a semi-submerged circular cylinder and a fixed and freely floating ship section in beam-sea waves. For the freely floating ship section, the present method is compared in detail with results from a dedicated study performed with a fully nonlinear boundary element method for cases with roll motions up to 30°. The present results are generally in good agreement with reference results, even for the most challenging wave–body interaction cases considered. Based on this, we later intend to use the method to examine in depth the importance of nonlinear effects in the interaction between waves and rigid bodies.

1. Introduction

For decades, the oil and gas industry has relied on drilling and production ships and platforms in harsh locations. Nowadays, coastal and offshore regions are populated by an increasing amount of fixed and floating structures. Wind turbines have been deployed in the water, first supported by bottom-fixed foundations and more recently as floating installations in deeper waters. Other innovative renewable-energy concepts, such as floating solar islands (Patterson et al., 2019), are proposed in coastal regions, and fish farms are moved away from fjords and into the ocean. By moving marine structures to more remote locations, they are exposed to more challenging wave conditions. Consider as an example offshore installations in the North Sea. These experience steep, essentially wind-generated sea states with significant wave heights larger than 15 m, and thus tremendous loads and wave-induced responses. Disregarding violent and partly local effects such as slamming, the structures are traditionally dimensioned by combining loads and responses from linear analysis tools with correction factors from hydrodynamic model tests and safety factors provided in rules and regulations. Slowly-varying wave loads are assumed to be of second order and either estimated from linear analysis using approximations (de Hauteclocque et al., 2012) or from a full second-order hydrodynamic analysis based on a perturbation approach. Using such efficient analysis tools is justified by the assumption that the structures' global behaviour is at most weakly nonlinear. However, the general validity of such hypothesis has been challenged during recent years. In some of the mooring line failures for floating structures in the North Sea documented over the last decades (Kvitrud, 2014a,b; Noble Denton Europe, 2006), exceedance of the mooring lines' strength capacity is identified as the failure mechanism. Although unintentional

* Corresponding author.
E-mail addresses: finn-christian.hanssen@ntnu.no (F.-C. W. Hanssen), marilena.greco@ntnu.no (M. Greco).

https://doi.org/10.1016/j.oceaneng.2021.108841
Received 10 December 2020; Received in revised form 11 February 2021; Accepted 28 February 2021

response of dynamic positioning systems may have played a role, it is suggested that the environmental loads, in particular the wave drift loads, could have been larger than the mooring systems were designed to withstand. As a consequence of these observations, Fonseca et al. (2016), Fonseca and Stansberg (2017b) and Fonseca et al. (2017) documented through systematic model tests that wave-drift loads may be significantly under-predicted by state-of-the-art computational design tools in severe sea states. The largest differences are observed for semi-submersibles and are mainly due to viscous effects. However, non-negligible differences may also be identified for ship-shaped structures, where viscous effects are of less importance compared to nonlinear inviscid effects. As discussed by Fonseca and Stansberg (2017a), the damping of slowly-varying motions may also be influenced by nonlinear effects.

With the knowledge that linear tools may be insufficient for existing structures in harsh sea states, together with the deployment of new complex structures in exposed locations, analysis tools properly accounting for nonlinear effects are needed. The aim of the present research is therefore (1) to develop an accurate and efficient numerical method to study nonlinear wave and wave–body interaction problems and (2) to provide fundamental insight into global nonlinear effects beyond the capability of linear and weakly nonlinear methods. Only two-dimensional (2D) scenarios are considered, however, the methods are developed with future extension to three dimensions (3D) in mind. The water is assumed incompressible and irrotational, and viscous effects are neglected, hence potential-flow theory can be used. The present paper is concerned with (1), whereas (2) will be addressed in a separate study.

Several authors have used fully nonlinear potential-flow models, mostly based on the boundary element method (BEM). These include Vinje and Brevig (1981) and Dommermuth et al. (1988), who performed numerical analysis of steep, overturning waves in finite water depth in 2D until the point where the overturning wave reattaches to the underlying surface. Beyond this point, potential-flow theory does not apply. Greco (2001) examined water-on-deck problems in 2D, typically relevant for floating production units in large waves. You (2012) studied wave loads on and motions of moored ships in finite water depth in both 2D and 3D. In addition to incident-wave problems, fully nonlinear BEMs have been used to analyse water-entry problems. For instance, Sun (2007) investigated water entry of 2D bodies, accounting for non-viscous flow separation and hydroelastic effects. Other numerical methods in connection with nonlinear potential-flow models include the finite element method (FEM) such as used by Wu and Eatock Taylor (1994), Eatock Taylor (1996) and Yan and Ma (2007); Ma and Yan (2009) and the finite difference method (FDM) such as used by Bingham and Zhang (2007), Engsig-Karup et al. (2009) and Ducrozet et al. (2010). A comprehensive overview of the early development of potential-flow numerical wave tanks is presented by Kim et al. (1999).

In the present work, we use the harmonic polynomial cell (HPC) method proposed by Shao and Faltinsen (2012, 2014b) to solve the Laplace equation for the velocity potential numerically. Using high-order harmonic polynomials to represent the solution, this method has the potential to solve a problem to a given numerical error more efficiently than alternative numerical methods. Moreover, it gives a global system with a diagonally-dominated coefficient matrix in a similar manner as the FDM that can be solved efficiently by iterative matrix solvers. Several authors have applied the method in 2D: Liang et al. (2015) studied various problems in marine hydrodynamics, including coupling with a local solution to deal with singular flows at sharp corners. Zhu et al. (2017) developed a nonlinear NWT for wave propagation. Strand (2018) modelled the flow inside a closed, flexible fish cage using linear theory. Wang et al. (2020) used the HPC method with local grid refinement to study strongly nonlinear phenomena such as overturning waves and water entry of a wedge, and applied an irregular-cell technique to avoid the drawbacks of using distorted cells. The method's accuracy was systematically investigated by Ma et al. (2018). Bardazzi et al. (2015) used a generalized HPC method to solve the Poisson equation in a viscous-flow Navier–Stokes (NS) solver, and further use in connection with viscous flows is currently investigated by the same research group. Fredriksen (2015) and Hanssen et al. (2019) coupled the HPC method with NS solvers using domain-decomposition (DD) approaches. Siddiqui et al. (2018) used a weak DD scheme to couple a nonlinear HPC-based potential-flow solver with the open-source NS solver OpenFOAM to investigate the flow inside a damaged ship compartment undergoing forced heave motions in still water. In 3D, the method has been used by Shao and Faltinsen (2014b,a) to investigate nonlinear wave-propagation and nonlinear run-up around upright bottom-mounted cylinders, and by Liang et al. (2020) to model sloshing inside an upright circular tank using an overset-mesh technique.

Immersed boundary methods (IBM) are traditionally not widely used in potential-flow solvers. However, using an IBM in field methods has significant attractive features, since it eliminates the need to fit grids to complex boundaries and update these as the boundaries move or deform with time. This may both be time consuming and result in poor-quality grids. Recently, Xu et al. (2020) demonstrated an IBM to model the free surface in a 2D FDM with promising results. In the HPC method, using an IBM to model physical boundaries was first attempted by Hanssen et al. (2015) in 2D using an approach that required auxiliary interpolation schemes to be constructed. Utilizing that the HPC method provides analytical expressions for the velocity potential anywhere in the fluid and not only in discrete nodes, the need for these auxiliary interpolation schemes was eliminated in the enhanced IBM by Hanssen et al. (2018). A similar IBM was used by Robaux and Benoit (2018, 2020) to investigate waves propagating over a submerged body and waves interacting with a fixed surface-piercing body, and by Shen et al. (2020) to model steep and even overturning sloshing waves inside a 2D closed fish cage with local grid refinement. Tong et al. (2021) used the IBM together with local grid refinement to model waves interacting with a surface-piercing body that is fixed or has prescribed motion. As an additional modelling concept, Hanssen et al. (2018) introduced an overlapping, body-fixed Cartesian grid to model the region close to a physical wavemaker. In the present work, we generalize this approach to include a surface-piercing body modelled with an IBM in a body-fixed, Cartesian grid in an extension of the work presented by Hanssen et al. (2017). The body may be fixed or undergo forced or freely-floating motion. In addition to combining the HPC method with immersed boundaries and overlapping grids in a novel way, this is to our knowledge the first published study where the HPC method is used to couple the hydrodynamic problem with the equations of rigid-body motion.

The rest of the paper is organized as follows: First, theoretical background related to body-fixed reference frames and potential-flow theory is given. Then, the implementation of the numerical method is described. Finally, comparisons against existing reference results for wave propagation and wave–body interaction are presented before main conclusions are drawn.

2. Theoretical framework

Relevant background for body-fixed reference frames and fundamental equations of potential-flow theory in inertial and body-fixed reference frames is outlined. Two-dimensional (2D) water waves and their interaction with a surface-piercing fixed or floating structure are considered.

2.1. Coordinate systems

A right-handed inertial, Earth-fixed coordinate Oxz system is introduced, where the z axis is positive in upward direction with origin in the mean water line. The Oxz system coincides with the xz plane of a right-handed three-dimensional (3D) $Oxyz$ system. Thus, angular

motions and moments are referred to as rotation about the y axis. Body-fixed coordinate systems $ox_{bf}z_{bf}$ are introduced for moving bodies, illustrated for a floating box-shaped structure in Fig. 1. The body-fixed coordinate system is complemented by a body-related coordinate system $ox'z'$ with origin coinciding with that of the $ox_{bf}z_{bf}$ system but axes parallel with the Oxz system. The wave–body interaction cases considered in the present paper are relevant for ships in beam-sea waves, and motions parallel to the x and z axes are hence denoted as sway and heave, respectively. Rotations α about the y axis are denoted as roll with positive direction indicated in Fig. 1.

A point $\boldsymbol{P} = (x_p, z_p)$ defined in the inertial Oxz coordinate system can be expressed in the body-fixed coordinate system by a two-step coordinate transformation consisting of

1. a coordinate displacement, where $\boldsymbol{P}$ is expressed in the body-related coordinate system as $\boldsymbol{P}' = (x'_p, z'_p)$, and
2. a coordinate rotation, where the coordinates are projected onto the axes of the body-fixed coordinate system.

The coordinate rotation uses a rotation matrix

$$\boldsymbol{\Lambda}(\alpha) = \begin{pmatrix} cos\alpha & sin\alpha \\ -sin\alpha & cos\alpha \end{pmatrix}, \tag{1}$$

where α is defined in Fig. 1 and given in radians. This gives the following relations: $\boldsymbol{P}_{bf} = (x_{p,bf}, z_{p,bf}) = \boldsymbol{\Lambda}_{i\to b} \cdot \boldsymbol{P}'$ and $\boldsymbol{P}' = \boldsymbol{\Lambda}_{b\to i} \cdot \boldsymbol{P}_{bf}$, where $\boldsymbol{\Lambda}_{i\to b} = \boldsymbol{\Lambda}(-\alpha)$ and $\boldsymbol{\Lambda}_{b\to i} = \boldsymbol{\Lambda}(\alpha)$. When rotating time derivatives of vector quantities between inertial and non-inertial coordinate systems, one must account for the time-rate of change of the unit vectors in the latter, e.g.

$$\dot{\boldsymbol{P}}' = \boldsymbol{\Lambda}_{b\to i} \cdot \dot{\boldsymbol{P}}_{bf} + \dot{\boldsymbol{\Lambda}}_{b\to i} \cdot \boldsymbol{P}_{bf}. \tag{2}$$

The overdot here means time derivative relative to the coordinate system that the quantity is defined in, i.e. $\dot{\boldsymbol{P}}'$ and $\dot{\boldsymbol{P}}_{bf}$ are the time derivatives of $\boldsymbol{P}'$ and $\boldsymbol{P}_{bf}$ in the inertial and body-fixed coordinate systems, respectively. The reason for taking the time derivative of $\boldsymbol{P}'$ in the inertial coordinate system is that the $ox'z'$ coordinate system is only displaced and not rotated relative to the Oxz coordinate system.

2.2. Kinematics

For a generic vector $\boldsymbol{s}$, the following notation is used hereafter:

- $d\boldsymbol{s}/dt$ is the time derivative of $\boldsymbol{s}$ in the inertial reference frame
- $\dot{\boldsymbol{s}}$ is the time derivative of $\boldsymbol{s}$ in the reference frame where it is defined
- a subscript bf explicitly means that the vector is projected along the axes of the $ox_{bf}z_{bf}$ system.

We now consider the point P in Fig. 1. The position and velocity of P in the Oxz coordinate system are given as

$$\boldsymbol{R} = \boldsymbol{R}_0 + \boldsymbol{r}, \tag{3}$$

$$\frac{d\boldsymbol{R}}{dt} = \frac{d\boldsymbol{R}_0}{dt} + \frac{d\boldsymbol{r}}{dt} = \dot{\boldsymbol{R}}_0 + \dot{\boldsymbol{r}} + \boldsymbol{\omega}\times\boldsymbol{r}, \tag{4}$$

where $\boldsymbol{\omega}$ is the angular velocity vector, in 2D given as $\boldsymbol{\omega} = \dot{\alpha}\boldsymbol{j}$ with $\boldsymbol{j}$ the unit vector in y direction. Noting that $\boldsymbol{\omega}\times\boldsymbol{\omega} = \boldsymbol{0}$ in 2D, the acceleration of P in the inertial reference frame is

$$\frac{d^2\boldsymbol{R}}{dt^2} = \ddot{\boldsymbol{R}}_0 + \boldsymbol{\omega}\times\dot{\boldsymbol{R}}_0 + \ddot{\boldsymbol{r}} + \dot{\boldsymbol{\omega}}\times\boldsymbol{r} + 2\boldsymbol{\omega}\times\dot{\boldsymbol{r}} + \boldsymbol{\omega}\times(\boldsymbol{\omega}\times\boldsymbol{r}). \tag{5}$$

If P is a fixed point on the body surface, the equations simplify to

$$\frac{d\boldsymbol{R}}{dt} = \dot{\boldsymbol{R}}_0 + \boldsymbol{\omega}\times\boldsymbol{r}, \tag{6}$$

$$\frac{d^2\boldsymbol{R}}{dt^2} = \ddot{\boldsymbol{R}}_0 + \boldsymbol{\omega}\times\dot{\boldsymbol{R}}_0 + \dot{\boldsymbol{\omega}}\times\boldsymbol{r} + \boldsymbol{\omega}\times(\boldsymbol{\omega}\times\boldsymbol{r}). \tag{7}$$

2.3. Time derivative of scalars

In addition to vectors, also the time derivative of scalar quantities generally differ in inertial and body-fixed reference frames (Faltinsen and Timokha, 2009). We define $D_{BO}q/Dt$ as the time derivative of a generic, time-dependent scalar q performed following the motion of a rigid body. If the time derivative is taken in P defined in Fig. 1, and the location of this point is fixed in $ox_{bf}z_{bf}$,

$$\frac{D_{BO}q}{Dt} = \frac{\partial q}{\partial t} + (\dot{\boldsymbol{R}}_0 + \boldsymbol{\omega}\times\boldsymbol{r})\cdot\nabla q. \tag{8}$$

Here, $\partial q/\partial t$ is the Eulerian time derivative of q, i.e. the time derivative of q in a fixed point in the inertial coordinate system.

2.4. The equations of motion

The translational motions of a rigid body follow from Newton's second law, which in the inertial reference frame is defined as

$$M\frac{d^2\boldsymbol{R}_0}{dt^2} = \boldsymbol{F}_{ext}. \tag{9}$$

Here, M is the body's mass, $\boldsymbol{F}_{ext}$ is the external force vector, which is the sum of all loads acting on the body including its weight, and $d^2\boldsymbol{R}_0/dt^2$ is the acceleration of the centre of gravity in the inertial reference frame. The equation may be rewritten in the body-fixed reference frame,

$$M(\ddot{\boldsymbol{R}}_{0,bf} + \boldsymbol{\omega}\times\dot{\boldsymbol{R}}_{0,bf}) = \boldsymbol{F}_{ext,bf}, \tag{10}$$

where $\boldsymbol{F}_{ext,bf} = \boldsymbol{\Lambda}_{i\to b}\cdot\boldsymbol{F}_{ext}$. It should be noted that additional terms apply in Eq. (10) if written for another point than the centre of gravity since then $\boldsymbol{r} \neq \boldsymbol{0}$. The equation of rotational motion in the inertial reference frame is

$$\boldsymbol{I}\cdot\dot{\boldsymbol{\omega}} + \boldsymbol{\omega}\times(\boldsymbol{I}\cdot\boldsymbol{\omega}) = \boldsymbol{M}_{ext} \tag{11}$$

with $\boldsymbol{I}$ the rotational inertia matrix and $\boldsymbol{M}_{ext}$ the total external moment vector. The term $\boldsymbol{\omega}\times(\boldsymbol{I}\cdot\boldsymbol{\omega})$ is challenging in 3D, because it implies that the body has a time-varying inertia. Shao (2010) avoided this challenge by formulating the problem in the body-fixed reference frame. In 2D, the equation of rotational motion is independent of reference frame and simplifies to

$$I_{yy}\ddot{\alpha} = M_{y,ext}, \tag{12}$$

where I_{yy} is the body's moment of inertia about the y axis and $M_{y,ext}$ the total external moment about the y axis.

2.5. Potential-flow theory

The water is assumed to be incompressible and inviscid with irrotational motion, so that the water velocity $\boldsymbol{V}$ can be expressed as the gradient of a velocity potential φ that satisfies the Laplace equation $\nabla^2\varphi(x,z,t) = 0$ (Faltinsen, 1993). The pressure $p(x,z,t)$ in the water relative to the atmospheric pressure is given by the Bernoulli equation,

$$p(x,z,t) = -\rho\left(\frac{\partial\varphi}{\partial t} + \frac{1}{2}|\nabla\varphi|^2 + gz\right), \tag{13}$$

where ρ is the mass density of water and g is the acceleration of gravity. If the time derivative of φ in the point P in Fig. 1 is estimated in the body-fixed reference frame, Eq. (8) may be used to rewrite Eq. (13) as

$$p(x_{bf}, z_{bf}, t) = -\rho\left(\frac{D_{BO}\varphi}{Dt} - (\dot{\boldsymbol{R}}_0 + \boldsymbol{\omega}\times\boldsymbol{r})\cdot\nabla\varphi + \frac{1}{2}|\nabla\varphi|^2 + gz\right). \tag{14}$$

The most straightforward way to estimate $\partial\varphi/\partial t$ in Eq. (13), or $D_{BO}\varphi/Dt$ in Eq. (14), is to use a backward finite-difference method. However, it was shown by Hanssen et al. (2015) that such finite-difference schemes may produce spurious temporal oscillations in the fluid pressure and hence in the integrated loads on a body. A more accurate method used

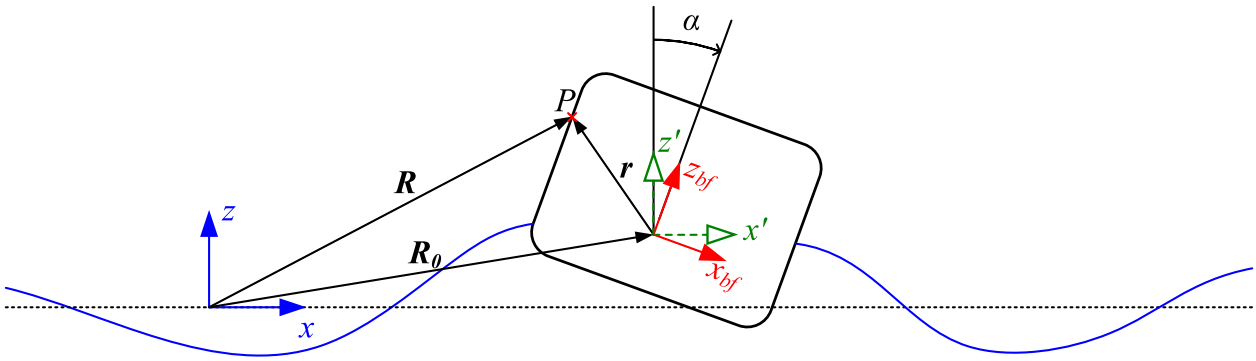

Fig. 1. Definition of a point P in the Oxz, $ox'z'$ and $ox_{bf}z_{bf}$ coordinate systems.

by e.g. Tanizawa (1995), Greco (2001), Koo and Kim (2004) and Sun (2007) is to formulate an auxiliary hydrodynamic problem for the time derivative of φ. This is possible because $\partial\varphi/\partial t$ and $D_{BO}\varphi/Dt$ satisfy the Laplace equation. In the present work, where we use mixed reference frames in overlapping grids, the numerical problem is formulated for $\partial\varphi/\partial t$ in grids modelled in the inertial reference frame and for $D_{BO}\varphi/Dt$ in grids modelled in body-fixed reference frames.

Hydrodynamic boundary-value problems

A principal sketch of a numerical domain consisting of the water volume inside a numerical wave tank (NWT) with a floating body is shown in Fig. 2. The mathematical boundary-value problems (BVP) to estimate φ and its time derivative inside Ω require that appropriate boundary conditions are specified along the closed surface (in 2D, Ω is strictly speaking bounded by a closed *curve* and not a surface).

The evolution of the free surface S_{SF} is described by tracking massless markers in time. Consider a marker with coordinates $(x,z) = (x,\zeta(x))$ in the inertial coordinate system and with velocity potential φ_ζ. At each time instant, Dirichlet conditions on the form $\varphi = \varphi_\zeta$ are enforced on S_{SF}. The values of φ_ζ and ζ are updated by integrating the dynamic and kinematic free-surface conditions (15) in time.

$$\begin{aligned}\frac{\delta\varphi_\zeta}{\delta t} &= -\frac{1}{2}|\nabla\varphi|^2 - gz + \boldsymbol{v}\cdot\nabla\varphi - \nu(x,t)(\varphi-\varphi_{ref})\\ \frac{\delta\zeta}{\delta t} &= \frac{\partial\varphi}{\partial z} + (\boldsymbol{v}-\nabla\varphi)\cdot\nabla\zeta - \nu(x,t)(\zeta-\zeta_{ref})\end{aligned} \quad \text{on} \quad S_{SF}. \tag{15}$$

$\delta/\delta t = \partial/\partial t + \boldsymbol{v}\cdot\nabla$ is a Lagrangian time derivative. With $\boldsymbol{v} = \boldsymbol{0}$, Eq. (15) represents an Eulerian formulation, $\boldsymbol{v} = \nabla\varphi$ gives a fully-Lagrangian formulation and $\boldsymbol{v} = (0, \partial\zeta/\partial t)$ gives a semi-Lagrangian formulation where the markers are restricted to move in the z direction. In the present work, the semi-Lagrangian formulation, requiring the least smoothing, is generally used for pure wave-propagation cases, while the fully-Lagrangian formulation, allowing wave–body intersection points to move without constraints, is used when analysing scenarios involving wave–body interactions. A special type of hybrid description is used in the analysis of a heaving semi-submerged circular cylinder, where the x-component of $\boldsymbol{v}$ is written as $\kappa(x)\partial\varphi/\partial x$. κ is set to unity at the wave-cylinder intersection points, giving a fully-Lagrangian description, and decreases linearly towards zero (semi-Lagrangian description) some distance away from the cylinder. $\nu(x,t)$ in Eq. (15) is a damping coefficient associated with dissipation zones (beaches) to prevent wave reflections. φ_{ref} and ζ_{ref} are reference values for the velocity potential and wave elevation, respectively. The body-fixed equivalent of Eq. (15) is given in Hanssen (2019). Dirichlet conditions for $\partial\varphi/\partial t$ and $D_{BO}\varphi/Dt$ on S_{SF} follow directly from Eqs. (13) and (14), noting that the pressure is atmospheric on the free surface (i.e. $p = 0$). On the remaining boundaries, Neumann conditions are imposed. In the inertial reference frame these are written

$$\nabla\varphi\cdot\boldsymbol{n} = \boldsymbol{U}\cdot\boldsymbol{n} \quad \text{on} \quad \{S_B, S_{Seabed}, S_{Wall}, S_{WM}\}, \tag{16}$$

where $\boldsymbol{n}$ is the normal vector defined in Fig. 2. The velocity of the boundary $\boldsymbol{U}$ is zero along S_{Seabed} and S_{Wall}. On S_B and S_{WM}, $\boldsymbol{U}$ is given by Eq. (6). Neumann conditions for $\partial\varphi/\partial t = \varphi_t$ along S_{Seabed} and S_{Wall} are found by taking the Eulerian time derivative of Eq. (16) in the inertial reference frame. Noting that $\partial\boldsymbol{n}/\partial t = \boldsymbol{0}$, this gives

$$\nabla\varphi_t\cdot\boldsymbol{n} = 0 \quad \text{on} \quad \{S_{Seabed}, S_{Wall}\}, \tag{17}$$

where we have used that $\partial(\nabla\varphi)/\partial t = \nabla(\partial\varphi/\partial t)$. Boundary conditions for the time derivative of φ along S_{Seabed} and S_{Wall} are always specified in the inertial reference frame. On S_B and S_{WM}, however, the mathematical formulation is simplified by specifying boundary conditions in the associated body-fixed reference frames. The Neumann conditions for $D_{BO}\varphi/Dt$ on these boundaries are derived by taking the time derivative of Eq. (16) following the motion of the body:

$$\frac{D_{BO}\nabla\varphi}{Dt}\cdot\boldsymbol{n} + \nabla\varphi\cdot\frac{D_{BO}\boldsymbol{n}}{Dt} = \frac{D_{BO}\boldsymbol{U}}{Dt}\cdot\boldsymbol{n} + \boldsymbol{U}\cdot\frac{D_{BO}\boldsymbol{n}}{Dt}. \tag{18}$$

Although the subscript bf is here omitted, it is implicit that all vectors are written in the body-fixed coordinate system. The normal vector $\boldsymbol{n}$ is hence time-independent, so that Eq. (18) becomes

$$\frac{D_{BO}\nabla\varphi}{Dt}\cdot\boldsymbol{n} = \frac{D_{BO}(\dot{\boldsymbol{R}}_0 + \boldsymbol{\omega}\times\boldsymbol{r})}{Dt}\cdot\boldsymbol{n}. \tag{19}$$

The final version of the boundary condition enforced in the body-fixed reference frames along S_B and S_{WM} thus reads

$$\nabla\frac{D_{BO}\varphi}{Dt}\cdot\boldsymbol{n} = (\ddot{\boldsymbol{R}}_0 + \dot{\boldsymbol{\omega}}\times\boldsymbol{r})\cdot\boldsymbol{n} \quad \text{on} \quad \{S_B, S_{WM}\}. \tag{20}$$

The change of operators from $D_{BO}(\nabla\varphi)/Dt$ to $\nabla(D_{BO}\varphi/Dt)$ is discussed by Hanssen (2019).

3. Numerical implementation

Using the theoretical framework introduced in the previous section, a fully nonlinear potential-flow numerical wave tank (NWT) is developed. Starting from an initial state with still water at $t = 0$, the free surface and rigid-body motion are evolved in time with a standard fourth-order Runge–Kutta (RK4) scheme using the free-surface conditions (15) and the equations of motion (10), (12). Numerically, the configuration and properties of the free surface are described by a finite number of markers that are tracked in time. After each RK4 sub step, the wave elevation ζ, and the velocity potential φ_ζ imposed as Dirichlet condition on the free surface, are updated for each marker. If there is a rigid body present, the position and velocity of this after each RK4 sub step result in updated body-boundary Neumann conditions. On the remaining boundaries, i.e. the flat seabed, the wavemaker and the downwave tank wall, Neumann boundary conditions are enforced. Hence, four BVPs for φ must be constructed and solved for each physical time step evolving the solution from t_n to $t_n + \Delta t$, where Δt is the time step. If there is a freely floating body present, four BVPs must also be solved for the time derivative of φ. On the other hand, if

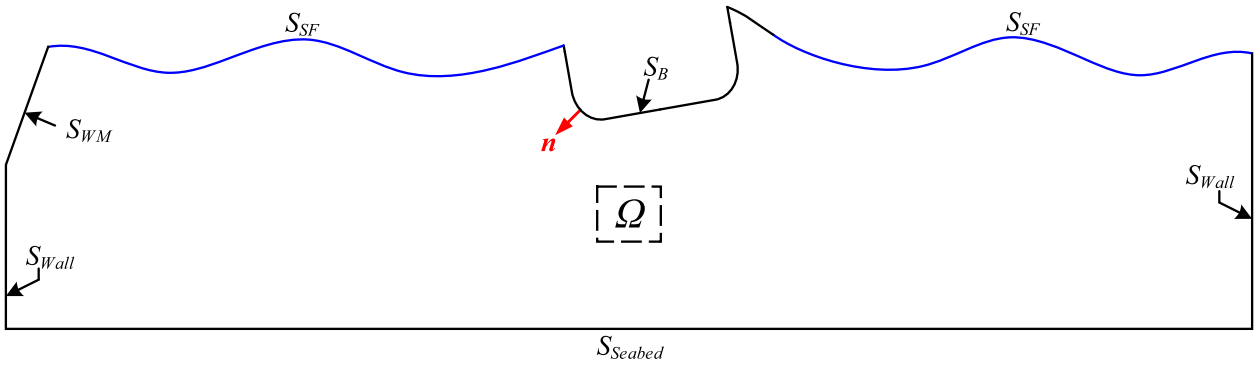

Fig. 2. Water domain Ω for hydrodynamic BVP bounded by the free surface S_{SF}, body boundary S_B, seabed S_{Seabed}, vertical tank walls S_{Wall} and wavemaker S_{WM}. The normal vector $\boldsymbol{n}$ is positive pointing into Ω.

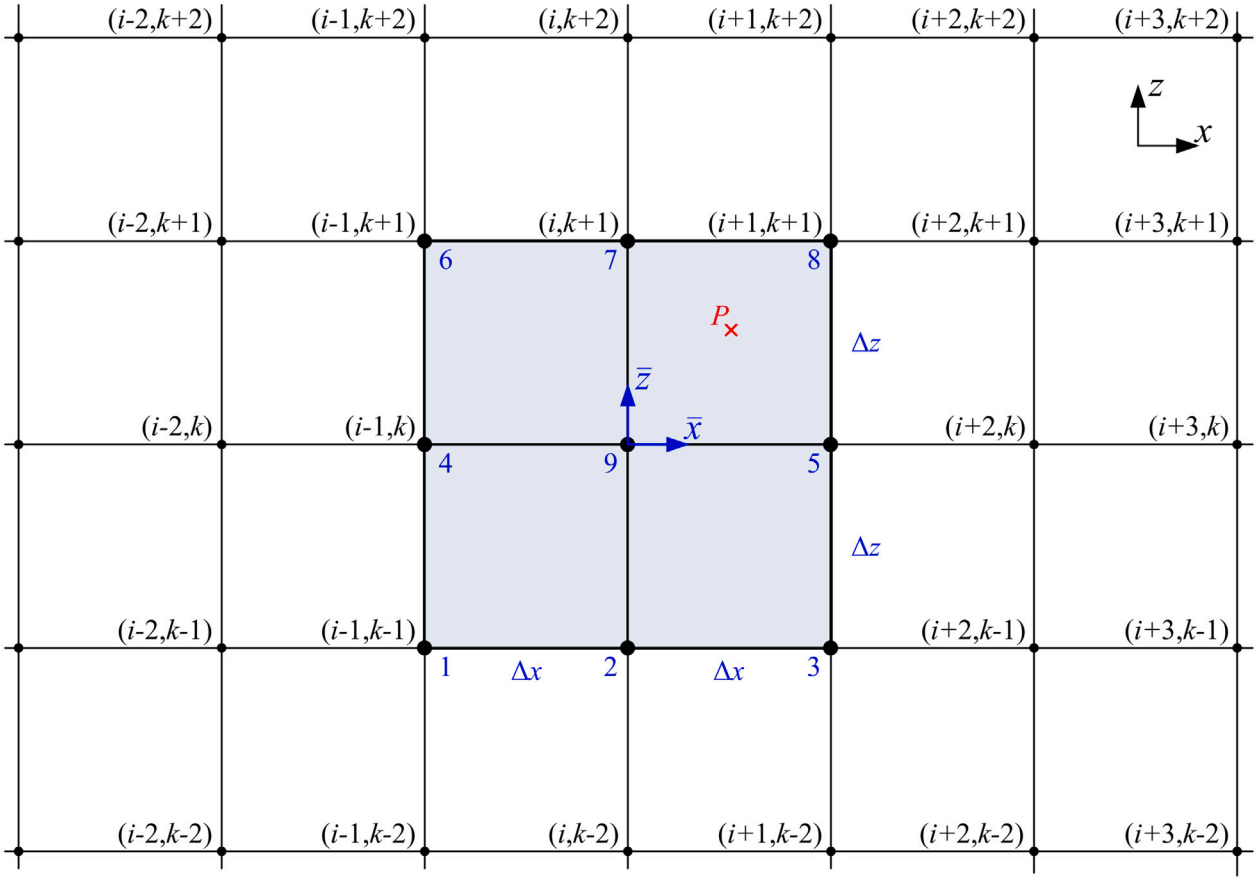

Fig. 3. HPC grid defined in the inertial Oxz coordinate system consisting of nodes with global indices (i, k) and overlapping cells. Each cell has a local cell-fixed coordinate system $o\overline{xz}$. The local node numbering in the highlighted cell is indicated with blue numbers.

the body undergoes forced motions, it is sufficient to solve the latter BVP only once at the end of each physical time step. This is because the body motions in this case are known and not integrated forward in time in the RK4 scheme.

The HPC method is used as a solver for the hydrodynamic BVPs, combining an IBM with overlapping, Cartesian grids to model complex surfaces and motions of rigid bodies. The combined method is denoted as an immersed boundary-overlapping grid method (IBOGM), and represents a novel development in connection with the HPC method. The "classical" 2D formulation of the HPC method and how it is implemented in the IBOGM are explained in the two following sections.

3.1. The harmonic polynomial cell method

The computational domain is divided into overlapping, quadrilateral cells as shown in Fig. 3 for a grid defined in the inertial coordinate system. The grid nodes have global horizontal and vertical indices denoted (i, k). Each cell is made up of eight boundary nodes numbered from 1 to 8 with grid spacing Δx and Δz in x and z direction, respectively. The interior node in each cell, which is a boundary node in any of the eight overlapping cells, is given local index 9. Each cell has a local cell-fixed coordinate system $o\overline{xz}$ with origin in this node so that $(\overline{x}, \overline{z}) = (x, z) - (x_9, z_9)$ with (x_9, z_9) the coordinates of the interior cell

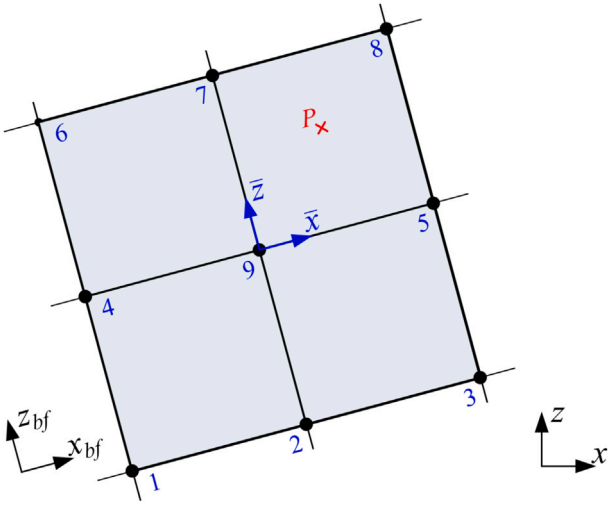

Fig. 4. HPC grid defined in a body-fixed $ox_{bf}z_{bf}$ coordinate system that is displaced and rotated compared to the inertial Oxz coordinate system.

node in the global coordinate system. In a grid specified in a body-fixed $ox_{bf}z_{bf}$ coordinate system as illustrated in Fig. 4, the local coordinates inside a cell are given as $(\overline{x},\overline{z}) = (x_{bf}, z_{bf})-(x_{9,bf}, z_{9,bf})$ with $(x_{9,bf}, z_{9,bf})$ the coordinates of the interior cell node in the body-fixed coordinate system.

Consider an arbitrarily located point P within the highlighted cell in either Fig. 3 or Fig. 4 with coordinates $\overline{\boldsymbol{P}} = (\overline{x}_P, \overline{z}_P)$ in the cell's local coordinate system. The velocity potential in this point is represented as a linear combination of the velocity potentials in the cell's boundary nodes, $\varphi_i, i = 1,\ldots,8$,

$$\varphi\left(\overline{x},\overline{z}\right) = \sum_{i=1}^{8}\left[\sum_{j=1}^{8} c_{j,i} f_j\left(\overline{x},\overline{z}\right)\right]\varphi_i. \tag{21}$$

Taking the gradient of Eq. (21) gives the velocity vector:

$$\nabla\varphi\left(\overline{x},\overline{z}\right) = \sum_{i=1}^{8}\left[\sum_{j=1}^{8} c_{j,i}\nabla f_j\left(\overline{x},\overline{z}\right)\right]\varphi_i. \tag{22}$$

In the origin of the local cell-fixed coordinate system, Eq. (21) becomes

$$\varphi_9 = \varphi(0,0) = \sum_{i=1}^{8} c_{1,i}\varphi_i, \tag{23}$$

and is used to enforce continuity of the solution throughout the computational domain. In Eqs. (21)–(23), $f_j(\overline{x},\overline{z})$ is either the real or imaginary part of the complex nth order harmonic polynomial $(\overline{x}+\mathrm{i}\overline{z})^n$ with $\mathrm{i} = \sqrt{-1}$. $c_{j,i}$ is an element of the inverse of the matrix $\boldsymbol{D}$ with elements $d_{i,j} = f_j(\overline{x}_i,\overline{z}_i)$, where $(\overline{x}_i,\overline{z}_i)$ are the coordinates of the ith boundary node. Since $f_j(\overline{x},\overline{z})$ satisfies the Laplace equation, so does automatically the representation of φ in Eq. (21). The same complete set of harmonic polynomials up to third order and incomplete set up to fourth order as used by Shao and Faltinsen (2012) is included in the expressions. The selection of harmonic polynomials is discussed by Ma et al. (2018), where it is concluded that this is generally the best choice for an eight-node cell. Because polynomials up to fourth order are included, a spatial accuracy up to fourth order can be expected. However, under certain conditions an even better spatial accuracy can be achieved (Ma et al., 2018).

Recognizing that φ_i are the only time-dependent variables in Eq. (21), we have that

$$\varphi_t\left(\overline{x},\overline{z}\right) = \sum_{i=1}^{8}\left[\sum_{j=1}^{8} c_{j,i} f_j\left(\overline{x},\overline{z}\right)\right]\varphi_{t,i} \tag{24}$$

and

$$\nabla\varphi_t\left(\overline{x},\overline{z}\right) = \sum_{i=1}^{8}\left[\sum_{j=1}^{8} c_{j,i}\nabla f_j\left(\overline{x},\overline{z}\right)\right]\varphi_{t,i}, \tag{25}$$

where $\varphi_{t,i} = \partial\varphi_i/\partial t$. In the interior cell node, Eq. (24) becomes

$$\varphi_{t,9} = \varphi_t(0,0) = \sum_{i=1}^{8} c_{1,i}\varphi_{t,i}. \tag{26}$$

Replacing $\varphi_{t,i}$ with $D_{BO}\varphi_i/Dt$, Eqs. (24)–(26) describe $D_{BO}\varphi(\overline{x},\overline{z})/Dt$ in a body-fixed formulation. It is reminded that $D_{BO}\varphi/Dt$ is the time derivative of φ following the motion of a body, which we may think of as an Eulerian-type derivative in the body-fixed reference frame. If mixed reference frames are used, this difference is accounted for by using Eq. (8):

$$\begin{aligned}\frac{D_{BO}\varphi(\overline{x},\overline{z})}{Dt} &= \sum_{i=1}^{8}\left[\sum_{j=1}^{8} c_{j,i} f_j\left(\overline{x},\overline{z}\right)\right]\varphi_{t,i} + \\ &(\dot{\boldsymbol{R}}_0 + \boldsymbol{\omega}\times\boldsymbol{r})\cdot\sum_{i=1}^{8}\left[\sum_{j=1}^{8} c_{j,i}\nabla f_j\left(\overline{x},\overline{z}\right)\right]\varphi_i.\end{aligned} \tag{27}$$

A similar expression is required to write $\partial\varphi/\partial t$ as a function of $D_{BO}\varphi/Dt$.

3.2. Immersed boundary-overlapping grid method

The HPC method is implemented using an immersed boundary method (IBM) combined with overlapping grids, and the resulting method is therefore referred to as an immersed boundary-overlapping grid method (IBOGM). The main reason for using these two modelling concepts is to facilitate an accurate and computationally efficient numerical implementation for general wave and wave-rigid body interaction problems. Such problems are characterized by non-stationary boundaries that may be described by complex geometries. Moreover, local refinements of the computational domain may be necessary. With the IBM, arbitrarily shaped boundaries can be modelled straightforwardly, while grids overlapping enables local refinement. A significant advantage of the IBOGM is that Cartesian grids with square cells can be used throughout, which is found to be crucial in order to take advantage of the higher-order accuracy offered by the HPC method (Ma et al., 2018).

A principal sketch of the layout of a NWT modelled using the IBOGM is show in Fig. 5. The coarse background grid, defined in the inertial reference frame, is fixed, whereas the body-fixed grids follow the motions of the wavemaker and floating body, respectively. Nevertheless, all grids are stationary in their respective reference frames, so that the coefficients $c_{j,i}$ in Eqs. (21)–(27) only need to be computed once, which is beneficial with respect to computational efficiency. Without the use of overlapping grids, local grid refinement close to moving boundaries would have been more complicated using only square cells, although promising results using quad-tree refinement techniques have recently been published.

The BVPs for φ and its time derivative lead to global matrix equations on the form $\boldsymbol{A}\cdot\boldsymbol{\varphi} = \boldsymbol{b}_{\varphi}$ and $\boldsymbol{A}\cdot\boldsymbol{\varphi}_t = \boldsymbol{b}_{\varphi_t}$, where $\boldsymbol{A}$ is a shared global coefficient matrix, $\boldsymbol{\varphi}$ and $\boldsymbol{\varphi}_t$ are vectors that contain the velocity potential and its time derivative, respectively, of all grid nodes in the computational domain and $\boldsymbol{b}_{\varphi}$ and $\boldsymbol{b}_{\varphi_t}$ are vectors with boundary conditions. $\boldsymbol{A}$ is a sparse and narrow-banded matrix dominated by entries of the continuity equation (23). An example of the structure of $\boldsymbol{A}$ is given later in Fig. 9.

Boundary conditions on physical boundaries

On the free surface, Dirichlet conditions for φ and its time derivative are enforced by evaluating Eqs. (21) and (24) in the most appropriate cells containing it, see Fig. 6(a). These cells are denoted free-surface ghost cells and are determined by first selecting free-surface ghost

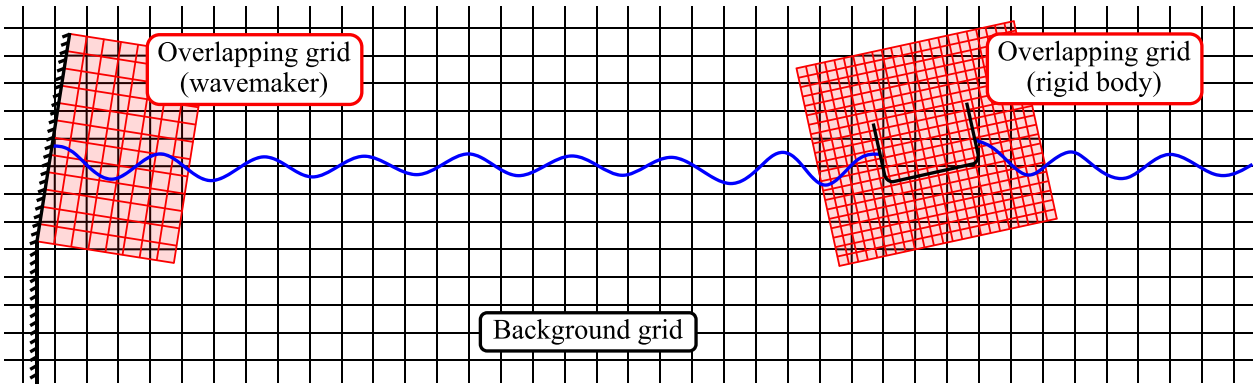

Fig. 5. Principal sketch of computational domain used in the IBOGM consisting of a background grid and overlapping grids that move with the motion of the wavemaker and of a generic 2D ship section, respectively.

nodes, which are the nodes just above the free surface. The ghost cells are the cells where the ghost nodes have local node number 7 (or 5 or 8 if the node is at rigid boundaries). Occasionally some additional ghost nodes must be introduced in the ghost cells in order to have the same number of unknowns and equations (rows) in $\boldsymbol{A}$. The number of free-surface Dirichlet conditions is equal to the number of ghost nodes. For each ghost node, the Dirichlet condition is enforced in the point on the free surface with the same x coordinate as the node if it belongs to the background grid, or with the same x_{bf} coordinate if the node is defined in an overlapping grid. If there are two ghost nodes with the same x (or x_{bf}) coordinate, this means that the boundary condition for the same point on the free surface is enforced twice. However, since the boundary conditions are enforced using different ghost cells, $\boldsymbol{A}$ does not become singular. If the free-surface markers are modelled with a fully-Lagrangian formulation, their positions will generally differ from the "vertical" grid lines, whereas if the semi-Lagrangian formulation is used the markers by definition move along the grid lines in z (or z_{bf}) direction. From a robustness point-of-view, it is found beneficial to enforce Dirichlet conditions in the locations where the free surface intersects the vertical grid lines. Therefore, in the fully-Lagrangian approach, third-order B-splines are used to interpolate the free-surface elevation and potential (in points that are not wave–body intersection points) to the x (or x_{bf}) coordinates of the grid nodes. These points are referred to as *evaluation points* in Fig. 7. One may wonder why this is done instead of using Eq. (21) to enforce Dirichlet conditions directly in the markers' position. Indeed, at a frozen time instant, this is allowed as long as there are enough markers located inside each cell. When attempting to use this approach in a simulation, however, free-surface instabilities rapidly occur. This is believed to be related to the fact that the accuracy of the numerical solution varies inside the cell, as was documented in 2D by Ma et al. (2018). They showed that the error of the numerical representation of φ in a cell is small along the vertical grid line through the centre of the cell, and with the B-spline interpolation, we are able to enforce boundary conditions for φ in these high-accuracy locations. It is found equally important that $\nabla\varphi$ is estimated with Eq. (22) in the same points as where the Dirichlet conditions for φ are enforced. Hence, we use third-order B-splines also to interpolate the values of $\nabla\varphi$ back to each of the markers where they are required in connection with the dynamic and kinematic free-surface conditions. Since the evaluation points coincide with the markers when the semi-Lagrangian formulation is used, no B-spline interpolation of free-surface properties is necessary in this case.

As illustrated in Fig. 7(a), when the semi-Lagrangian formulation is used, each grid has its separate set of free-surface markers. Markers that belong to the background grid inside one of the overlapping grids are in this case inactive with properties interpolated from the markers in the overlapping grid. With this approach, the free surface is a single, continuous boundary no matter if the semi-Lagrangian or fully-Lagrangian description is used.

For nodes on the tank walls, seabed, wavemaker and surface-piercing body, Neumann boundary conditions are enforced through Eqs. (22) and (25). For the moving wavemaker and body, the equations are applied in body-fixed reference frames. The body has an arbitrary geometry and generally does not intersect nodes in the body-fixed grid, and is hence modelled as an immersed boundary in this. Boundary conditions are enforced in discrete points along the boundary, using body-boundary ghost cells that contain the points (red-shaded cells in Fig. 6(b)). The algorithm used to deal with body boundaries here is as follows: First, body-boundary ghost nodes inside the body are selected. For each of these, the discrete point on the wetted part of the body closest to the ghost node is selected. We make sure that the same point on the body boundary is not used several times, which may lead to a singular matrix system. Finally, we select the most appropriate ghost cell to be used to enforce the body-boundary condition in the selected point. A reasonable choice of ghost cells is found to be characterized by that the ghost cells overlap, and that the majority of their area is outside the body. Using the IBM in the body-fixed grid, the procedure of identifying body-boundary ghost cells only has to be performed once at the start of the simulation. However, during the simulation it may happen that the pre-selected body-boundary points come above the instantaneous free surface. In this case, the body-boundary conditions related to these are instead enforced in body-boundary points just below the free surface.

The green-shaded cell in Fig. 6(b) is denoted a double cell used to enforce the free-surface Dirichlet and body-boundary Neumann conditions in the wave–body intersection point with coordinates (x_{WBI}, z_{WBI}) simultaneously. Denoting the local node indices in this cell 1–8, a set of fictitious nodes 1′–8′ are introduced with the same locations. The double cell contains a double node with local index k' (i.e. a replica of the node with local index k), which is the green node in the example in Fig. 6(b). Using the node with index k and the cell with local node indices 1–8, we enforce free-surface Dirichlet conditions in the point (x_{WBI}, z_{WBI}) through Eqs. (21) and (24). Similarly, we use the node with index k' and the cell with indices 1′–8′ to enforce Neumann conditions in (x_{WBI}, z_{WBI}) through Eqs. (22) and (25). In addition we enforce $\varphi_{i'} = \varphi_i$ and $D_{BO}\varphi_{i'}/Dt = D_{BO}\varphi_i/Dt$ for $\{i = 1, \ldots, 8, i \neq k\}$. The intention of the double cells is to introduce additional unknowns that enable us to enforce more than one boundary condition per wave–body intersection point. However, it is noted that the results applying this technique are found to be in close agreement with the results obtained only applying free-surface Dirichlet conditions in (x_{WBI}, z_{WBI}) for reasons that require a dedicated theoretical study that is not part of the present work. It is also noted that the water velocity used in the dynamic and kinematic free-surface conditions (15) is estimated using the double cells where the Dirichlet free-surface condition is enforced. Instead using the double cells where the Neumann body-boundary condition is enforced, i.e. the cells with indices 1′–8′, may give some non-physical spurious oscillations.

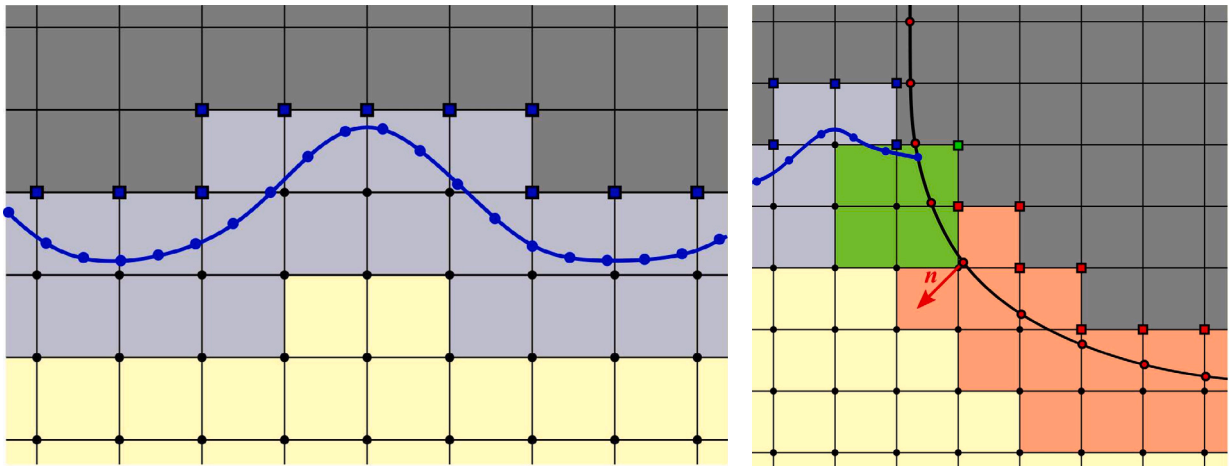

Fig. 6. Portion of free surface tracked with massless markers immersed in an inertial background grid (a) and body boundary immersed in an overlapping, body-fixed grid (b). Yellow and grey cells constitute the active and inactive parts of the computational domain. The black nodes below the free surface are interior cell nodes where Eqs. (23) and (26) are enforced. In the blue ghost cells the free-surface Dirichlet conditions are enforced through Eqs. (21) and (24) and in the red ghost cells body-boundary conditions are enforced through Eqs. (22) and (25) in the discrete points indicated with red circles. The green cell is a double cell where the free-surface and body-boundary conditions are enforced simultaneously in the wave–body intersection point. The blue and red square nodes are ghost nodes outside the physical domain, while the green node is a ghost node for both the free surface and body boundary. (For interpretation of the references to colour in this figure legend, the reader is referred to the web version of this article.)

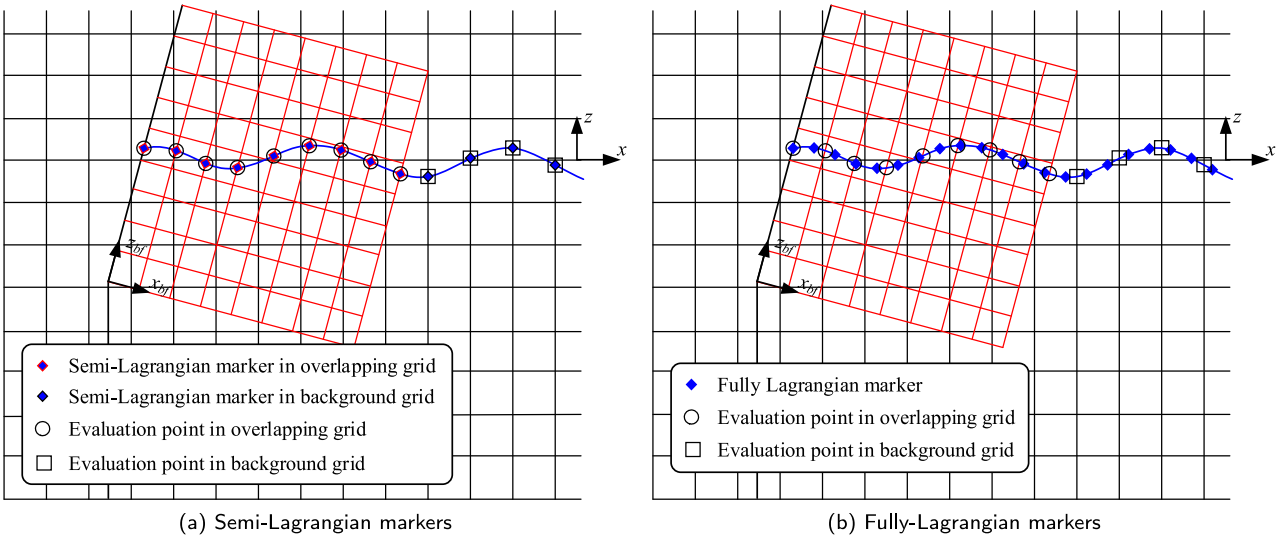

Fig. 7. Position of free-surface markers and evaluation points on the free surface. The latter points are where Dirichlet boundary conditions are enforced using Eqs. (21), (24), and where the water velocities are evaluated in connection with the kinematic and dynamic free-surface conditions (15).

An obvious consequence of using ghost cells in Fig. 6 is that a numerical solution exists outside the physical domain. It is important to point out that this solution has no physical meaning other than ensuring that the enforced boundary conditions are satisfied.

Coupling between grids

Continuity of the solution between the background grid and the overlapping grids is ensured through an implicit two-way coupling. For φ, this is provided by using Eq. (21), while for its time derivative equation (27) is used to account for the mixed reference frames. The coupling is illustrated in Fig. 8. In selecting cells used to interpolate the solution between the grids, care is taken to avoid recurrence. Recurrence here means that a cell in the background grid used to interpolate the solution in an overlapping grid contains nodes that have their solution interpolated from the overlapping grid and vice versa. An effective way to avoid this is to let the red nodes in Fig. 8(a) be some minimum distance away from the red nodes in (b). This distance should at least be equal to the largest grid spacing in any of the two grids.

A consequence of the IBM and the coupling between grids is that $\boldsymbol{A}$ changes with time because the number of nodes in the computational domain and their associated equations vary with time. Consequently, $\boldsymbol{A}$ must be built every time step. As it will later be discussed in connection with Fig. 14, this operation amounts to a large portion of the overall computational time. An example of $\boldsymbol{A}$ is given in Fig. 9. Although some non-zero off-diagonal entries exist due to coupling between the different grids, the matrix is diagonally-dominated and the global matrix equations can be efficiently solved by iterative solvers for sparse matrix systems. In the present work, a *bicgstab* solver with tolerance $5 \cdot 10^{-9}$ is used with a *splu* decomposition of $\boldsymbol{A}$ as pre-conditioner. This solver is part of the *SciPy* Python library, and gives stable and efficient solutions of the global matrix equations.

Integration of pressure

When φ and its time derivative are obtained from the solution of the hydrodynamic BVPs, the pressure is computed using the body-fixed version of the Bernoulli equation (14) in a set of discrete points

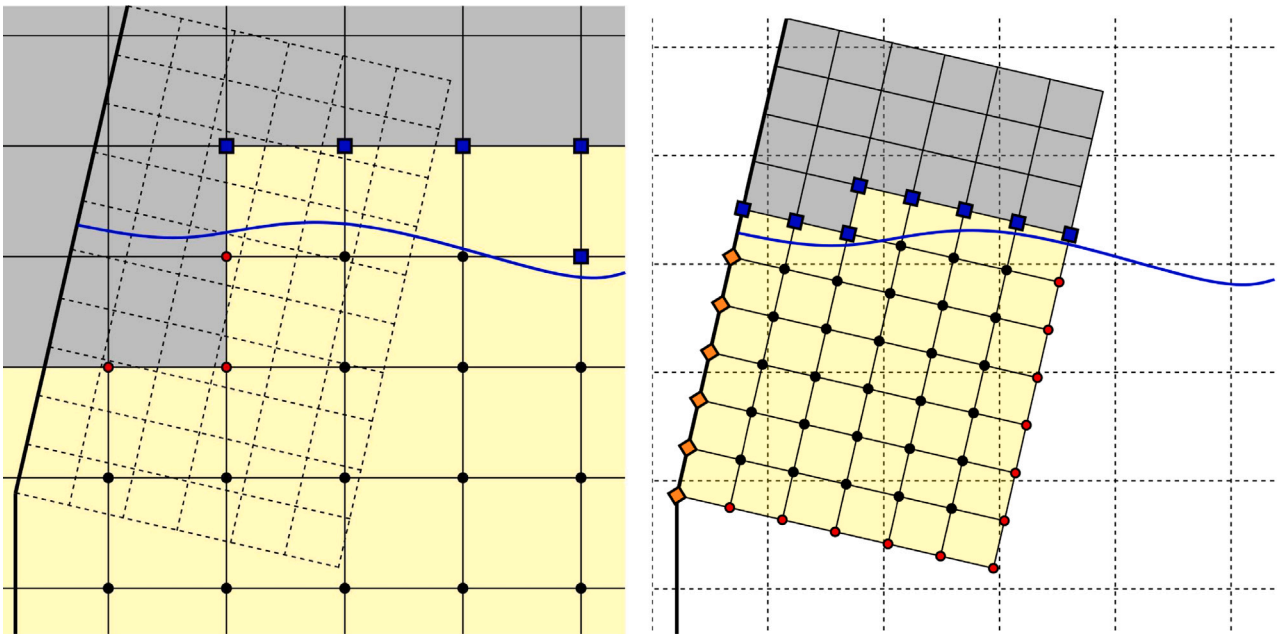

Fig. 8. Coupling between background grid and body-fixed grid on a flap-type wavemaker. The nodes indicated with red circles in (a) are where the solution in the background grid is interpolated from cells in the body-fixed grid, and in (b) where the solution in the body-fixed grid is interpolated from cells in the background grid. The nodes indicated with orange diamonds are where Neumann boundary conditions are enforced. The remaining node types are similar as in Fig. 6.

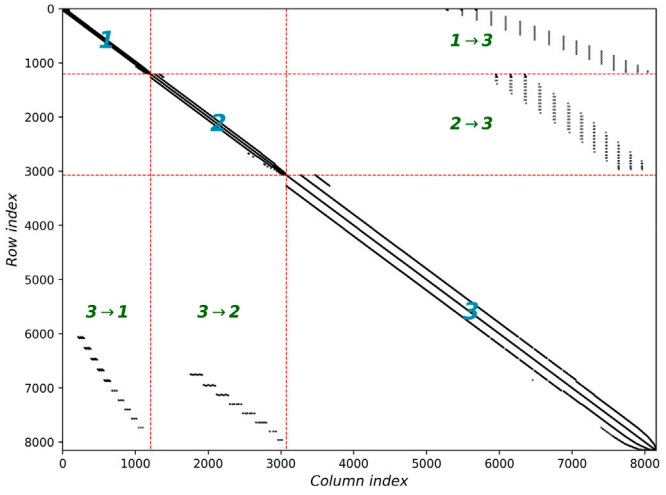

Fig. 9. Example of non-zero entries in global coefficient matrix. The body-fixed grids on the wavemaker and the body are for brevity denoted as 1 and 2, while the background grid is denoted as 3. $1 \rightarrow 3$, $3 \rightarrow 1$, $2 \rightarrow 3$ and $3 \rightarrow 2$ indicate coupling terms between the grids.

on the body boundary. The body boundary is here parametrized by a tangential coordinate s in anti-clockwise direction. Forces and moment are obtained by integrating the pressure over the instantaneous wetted body surface, $s_0 \leq s \leq s_1$:

$$\boldsymbol{F}_{bf}(t) = -\int_{s_0}^{s_1} p(s,t)\boldsymbol{n}_{bf}(s)ds, \tag{28}$$

$$M_y(t)\boldsymbol{j} = -\int_{s_0}^{s_1} p(s,t)(\boldsymbol{P}_{bf}(s) \times \boldsymbol{n}_{bf}(s))ds. \tag{29}$$

$\boldsymbol{P}_{bf}(s)$ represents the body-fixed coordinates of the point with tangential coordinate s relative to the centre of gravity. A negative sign appears in front of the integrals because the normal vector $\boldsymbol{n}_{bf}$ is defined outwards. M_y is independent of reference frame in 2D, while the force vector can be expressed in the inertial reference frame as $\boldsymbol{F} = \boldsymbol{\Lambda}_{b\rightarrow i} \cdot \boldsymbol{F}_{bf}$.

In the case of a freely floating body, the body motions are coupled with the fluid dynamic problem. This is highlighted by the fact that the pressure forces and moments are needed to estimate the body accelerations from the equations of motion (10), (12) but, at the same time, the pressure depends on the time derivative of φ that is obtained by solving a BVP where the same accelerations give the body-boundary conditions. This principally means that the body accelerations appear in both sides of the equations of motion. This coupling is handled here through the iterative scheme illustrated in Fig. 10, where the vector $\ddot{\boldsymbol{\Theta}}$ contains the translational and angular accelerations in the body-fixed reference frame. The input to each iteration loop is a guess of $\ddot{\boldsymbol{\Theta}}$ denoted as $\ddot{\boldsymbol{\Theta}}^0$, initially estimated using backward finite difference. The iteration is terminated when the error ϵ, having the dimension of the acceleration term with the largest individual error, is less than some predefined value ϵ_{tol}. The reason for using an absolute rather than a relative error as termination criterion is that the latter may lead to a slow convergence, or even divergence, when the accelerations are close to zero. With $\epsilon_{tol} = 10^{-3}$, which is found to be a reasonable value for the cases considered here, the number of iterations is typically in the order of five. The iteration scheme is efficient since it is only performed at the end of every physical time step, and because it introduces no changes to the coefficient matrix $\boldsymbol{A}$ or its pre-conditioner matrix. Only the elements in the right-hand side vector $\boldsymbol{b}_{\varphi_i}$ corresponding to body-boundary conditions for $D_{BO}\varphi/Dt$ require updating. Alternatively, the coupling between the body motions and the fluid dynamic problem can be handled intrinsically without iteration, for example with the mode-decomposition and indirect methods used by Koo and Kim (2004) or the implicit method proposed by Tanizawa (1995). However, these methods were developed for BEM solvers with collocation points distributed over the body surface, and using these techniques in the IBOGM is likely related with challenges. Taking the implicit method as an example, this requires that the integrals in Eqs. (28), (29) are implicitly written into $\boldsymbol{A}$ in a modified coefficient matrix $\boldsymbol{A}'$. Since $\boldsymbol{A}' \neq \boldsymbol{A}$, the same pre-conditioner matrix cannot be used as in the

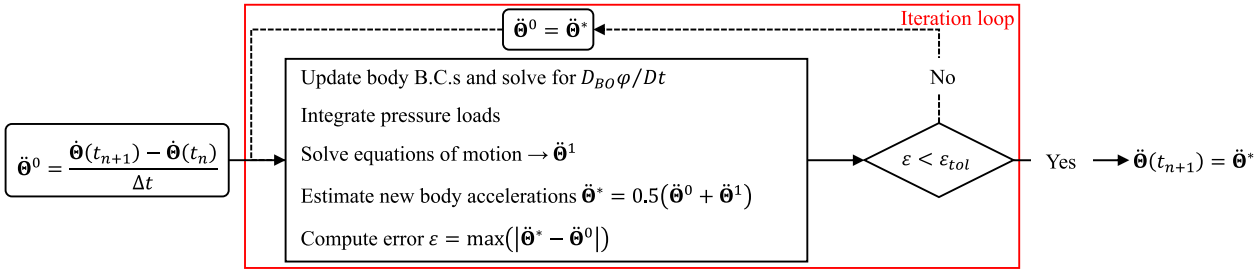

Fig. 10. Iteration loop to estimate body accelerations consistent with the coupling between body motions and fluid dynamic problem.

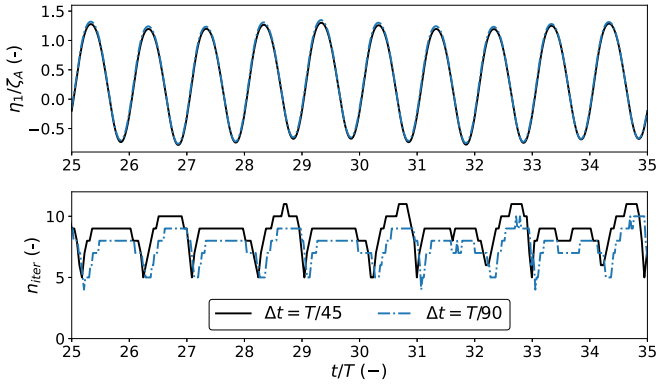

Fig. 11. Time series of surge motion η_1 (top) and number of iterations n_{iter} (bottom) as a function of time when nearly steady-state conditions are achieved for the case with $\xi_B = 0.5$ to be discussed in Section 4.4 for two different time steps Δt. ζ_A and T are the amplitude and period of the incident wave.

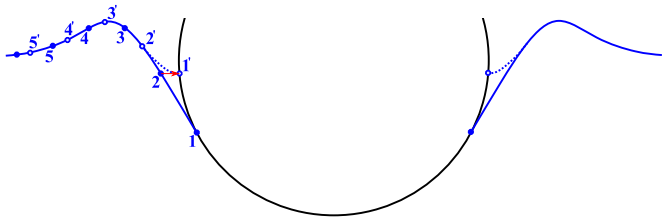

Fig. 12. Jet-cutting scheme illustrated for a scenario with small exterior angles. The blue filled markers are prior to jet-cutting while the white markers with blue borders are new marker locations after jet-cutting.

BVP for φ, and the additional terms written into $\boldsymbol{A}'$ reduce the sparsity compared to $\boldsymbol{A}$. These two aspects may contribute adversely to the computational efficiency. Moreover, including the boundary integrals over the surface of the body in $\boldsymbol{A}'$ is expected to influence the numerical stability in an IBM, especially when the rigid-body motions are large. To robustly include such non-iterative methods in the IBOGM therefore requires a dedicated effort, and is not pursued in the present work.

The convergence of the iterative body-acceleration scheme is investigated in Fig. 11 for one of the most numerically challenging freely-floating body cases that will be discussed in Section 4.4. Here, the surge motion obtained using 45 time steps per incident wave period is in good agreement with results using 90 time steps per wave period. This is also the case for the heave and roll motions, and 45 time steps per wave period therefore give sufficiently converged results. For this case, the average number of iterations n_{iter} is around eight with the largest time step Δt. n_{iter} is reduced when Δt is reduced, which indicates that the iterative scheme performs as intended; when the time step is reduced we expect smaller inconsistencies between the body accelerations and pressure loads, requiring fewer iterations.

$\boldsymbol{F}_{bf}$ and M_y in Eqs. (28), (29) are part of the external loads in the right-hand sides of the equations of motion (10) and (12). The external force vector also includes the vertical gravity force and possibly stiffness and linear damping forces,

$$\boldsymbol{F}_{bf,ext} = \boldsymbol{F}_{bf} - \boldsymbol{\Lambda}_{i\to b} \cdot (M g \boldsymbol{k}) - \boldsymbol{\Lambda}_{i\to b} \cdot (\boldsymbol{B}^l \cdot \dot{\boldsymbol{R}}_0 + \boldsymbol{C} \cdot \boldsymbol{R}_0), \tag{30}$$

where $\boldsymbol{B}^l$ is a linear damping matrix, $\boldsymbol{C}$ is a stiffness matrix and $\boldsymbol{R}_0 = \eta_1 \boldsymbol{i} + \eta_3 \boldsymbol{k}$. η_1 and η_3 are sway and heave motions in the inertial coordinate system, where $\boldsymbol{i}$ and $\boldsymbol{k}$ are unit vectors along the x and z axes, respectively. The external moment may include linear and quadratic roll damping,

$$M_{y,ext} = M_y - B^l_{\eta_5} \dot{\eta}_5 - B^q_{\eta_5} \dot{\eta}_5 |\dot{\eta}_5|, \tag{31}$$

where $B^l_{\eta_5}$ and $B^q_{\eta_5}$ are linear and quadratic damping coefficients and η_5 is the roll motion in radians.

Special treatment of wave–body intersection points

Using markers to track the free-surface evolution, it is important to prevent that the markers on wave–body intersection points separate from the body boundary, especially when the body geometry is non-vertical in the free surface region. This is ensured by reformulating the fully-Lagrangian version of the kinematic free-surface condition (15) in the tangential coordinate s defined in connection with Eqs. (28), (29):

$$\frac{Ds}{Dt} = \sigma_z |\nabla\varphi - \boldsymbol{u}_b|. \tag{32}$$

Here $\boldsymbol{u}_b$ is the velocity of the body surface in the marker location given by Eq. (6) and σ_z is the component in the z_{bf} direction of a sign function defined as $-sign(\nabla\varphi - \boldsymbol{u}_b)$ if the intersection point is on the left side of the body and as $sign(\nabla\varphi - \boldsymbol{u}_b)$ on the right side of the body. Since the wave–body intersection points are managed in the body-fixed reference frame, $\nabla\varphi - \boldsymbol{u}_b$ expresses the velocity-magnitude of the wave–body intersecting marker relative to this frame. The argument allowing us to use Eq. (32) is that, since Neumann conditions enforcing zero relative normal velocity between the water and body are applied in the wave–body intersection points, the markers' trajectories by definition have to be tangential to the surface.

In some scenarios, such as when the semi-submerged circular cylinder discussed later is forced to oscillate at a high frequency in heave, small angles between the free surface and the body surface can occur. If these angles become too small they may cause numerical instabilities. To promote numerical robustness, a jet-cutting scheme is therefore invoked when either the interior or exterior angle between free surface's and body boundary's tangents become less than 5°. The jet-cutting scheme is illustrated in Fig. 12: Marker 1 is removed, marker 2 is projected normally onto the body and a new marker is introduced between marker 2 and 3. The markers are then redistributed to ensure equal horizontal spacing. The markers before and after the jet-cutting are denoted 1–5 and 1′–5′, respectively.

Reduction of free-surface instabilities

Especially when using the fully-Lagrangian formulation of Eq. (15), instabilities may develop on the free surface. To prevent this, the third-order five-point filter used by Sun (2007) is applied to the free-surface elevation and velocity potential after every complete time step. In addition the fully-Lagrangian markers are redistributed with even

horizontal spacing so that they do not cluster together. With the semi-Lagrangian formulation of Eq. (15), Hanssen et al. (2018) found that a weaker twelfth-order Savitzky–Golay filter (Savitzky and Golay, 1964) is sufficient.

Wave generation and absorption

Waves are generated with a moving (physical) wavemaker of either a piston or flap type, where the former is typically used to generate shallow-water waves and the latter to generate waves in intermediate and deep water. A temporal ramp function $r_{wm}(t)$, defined as $0.5[1 - \cos(\pi t)/T_{ramp}]$ if $t \leq T_{ramp}$ and 1.0 otherwise, is introduced to avoid numerical instabilities due to an impulsive start of the wavemaker. T_{ramp} is the ramp function's duration, typically taken between three and five times the characteristic wave period. Considering a flap wavemaker with steady-state angular motion $\overline{\alpha}_{wm}(t)$, the flap signal used in a simulation is thus $\alpha_{wm}(t) = \overline{\alpha}_{wm}(t) r_{wm}(t)$. Waves are absorbed at numerical beaches modelled through the damping coefficient $\nu(x,t)$ in Eq. (15). Because reflected and radiated waves do not decay with distance in 2D, dissipation zones are necessary both towards the wavemaker (*upwave*) and the tank wall in the opposite (*downwave*) side. The purpose of the upwave beach is to dissipate waves propagating back towards the wavemaker, and φ_{ref} and ζ_{ref} in Eq. (15) are hence estimated from linear wavemaker theory (see e.g. Dean and Dalrymple, 1991). It was demonstrated by Hanssen (2019) that this approach gives satisfactory results, meaning that the fully nonlinear solution is retained a short distance away from the beach. An advantage of using linear theory is that both regular and irregular waves can be accounted for in a straightforward manner. The purpose of the downwave beach is to prevent any wave reflections from the tank wall, hence φ_{ref} and ζ_{ref} are equal to zero for this beach. $\nu(x,t)$ can be decomposed into a spatial and temporal contribution, $\nu(x,t) = \nu(x)\delta(t_0)$, where $\delta(t_0)$ is a step function which is zero for $t \leq t_0$ and 1 for $t > t_0$. t_0 is zero for the downwave beach, and is chosen larger than the time when transient waves associated with start-up of the wavemaker have propagated out of the beach for the upwave beach. $\nu(x)$ follows the definition in (Greco, 2001),

$$\nu(x) = \begin{cases} 0 & x \leq x_0 \\ \nu_{max}(-2\xi^3 + 3\xi^2) & x_0 < x \leq x_1 \text{ (downwave)} \\ \nu_{max}(1 + 2\xi^3 - 3\xi^2) & x_0 < x \leq x_1 \text{ (upwave)} \\ \nu_{max} & x > x_1, \end{cases} \tag{33}$$

where ν_{max} is an empirically chosen coefficient. x_0 and x_1 are the start and endpoints, respectively, of the beach. ξ is an auxiliary normalized coordinate defined as $\xi = (x - x_0)/L_{beach}$ where $L_{beach} = x_1 - x_0$ is the beach length. As a general guidance L_{beach} can be taken as two times the characteristic wavelength. Reasonable values for ν_{max} are generally found to be in the range 2–4 s^{-1}. If L_{beach} is too short, this may require a large ν_{max}, which can lead to wave reflections from the beach itself.

Schematic summary of solution algorithm

The flowchart in Fig. 13 illustrates the main steps involved in evolving the numerical solution from the known state at time t_n to the unknown state at $t_{n+1} = t_n + \Delta t$ for a freely-floating body case. Δt is here the constant time step. For a general solution variable y with time derivative given in the form $\dot{y} = \dot{y}(y,t)$, the RK4 time-integration scheme can be expressed as

$$y_{n+1} = y_n + \frac{\Delta t}{6}(k_{1,y} + 2k_{2,y} + 2k_{3,y} + k_{4,y}) \tag{34}$$

with coefficients $k_{i,y}, i = 1, \ldots, 4$:

$$\begin{aligned} k_{1,y} &= \dot{y}(y_n, t_n), \\ k_{2,y} &= \dot{y}(y_n + 0.5\Delta t k_{1,y}, t_n + 0.5\Delta t), \\ k_{3,y} &= \dot{y}(y_n + 0.5\Delta t k_{2,y}, t_n + 0.5\Delta t), \\ k_{4,y} &= \dot{y}(y_n + \Delta t k_{3,y}, t_n + \Delta t). \end{aligned} \tag{35}$$

In Fig. 13, the vectors $\boldsymbol{\varphi}$ and $\boldsymbol{\varphi}_t$ contain the velocity potential and its time derivative in all active grid nodes. These are obtained from solving the global matrix equations corresponding to the hydrodynamic BVPs. $\tilde{\boldsymbol{\varphi}}$ and $\tilde{\boldsymbol{x}}$ contain the velocity potential and position of all free-surface markers. The time derivatives of these are estimated from the dynamic and kinematic free-surface conditions (15). If the semi-Lagrangian versions of the free-surface conditions are used, only the vertical components in $\tilde{\boldsymbol{x}}$ are involved in the RK4 scheme. If instead the fully-Lagrangian versions of the free-surface conditions are used, the markers are redistributed with even spacing in horizontal direction after each complete RK4 cycle. The vector $\boldsymbol{\Theta} = (\boldsymbol{R}_0, \alpha)$ contains the translational and angular rigid-body motions, and the double time derivative of $\boldsymbol{\Theta}$, i.e. the rigid-body accelerations, are estimated from the equations of motion. An asterisk indicates the state of a variable or matrix after one of the three fictitious Euler steps involved in the RK4 scheme. For each physical time step, four hydrodynamic BVPs must be solved for φ together with $4 + n_{iter}$ BVPs for the time derivative of φ.

Computational effort

The computational effort involved in the different parts of the IBOGM is discussed using one of the freely-floating body cases that will be presented in Section 4.4 as example. As Fig. 14 shows, building the global matrix equation for φ accounts for more than 20% of the total CPU time. The majority of this time is spent to generate $\boldsymbol{A}$, since the size and topology of $\boldsymbol{A}$ inevitably change with time in the IBOGM. Recognizing that the majority of $\boldsymbol{A}$ is populated by entries of the connectivity Eq. (23), a useful technique that has been used here to limit the time spent constructing $\boldsymbol{A}$ is to initially generate a reservoir coefficient matrix $\boldsymbol{A}^*$ where Eq. (23) is inserted for all grid nodes except for those that are on boundaries. At any given time, relevant parts of $\boldsymbol{A}^*$ are copied into the correct locations in $\boldsymbol{A}$. Without this technique, the time to construct $\boldsymbol{A}$ increases notably. Generating the right-hand side vector for the global matrix equation of the time derivative of φ amounts to a little more than 10% of the total CPU time. It is noted that this vector is not entirely rebuilt for each of the cycles in the iterative scheme in Fig. 10; only the entries for body-boundary ghost nodes are updated when a new body acceleration is estimated. The time used by the iterative matrix solver, including generation of pre-conditioner matrices, amounts to more than 25% of the total time, while estimating and integrating the pressure over the wetted body surface amounts to a little less than 10% of the total CPU time. Since the pressure has to be integrated in each loop of the iterative scheme in Fig. 10, this time is significantly reduced if the body has prescribed motions. Moreover, it is expected that the time can be further reduced by optimizing the reuse of HPC expressions that do not change during the iterations. The remaining tasks in the *other* group in Fig. 14 include writing post-processing files, transforming coordinates between different coordinate systems and more. It is expected that the method's CPU time can be further reduced, and this will be increasingly important when extending from 2D to 3D.

4. Validation and verification

Validation and verification studies, comparing results against experimental, numerical and theoretical reference results are presented hereafter. First the solver's ability to propagate waves with nonlinear characteristics are considered. Thereafter, cases with rigid bodies (1) forced to oscillate in still water (radiation) and (2) kept fixed in incident waves (diffraction) are investigated. Finally, all aspects of the solver are combined for a freely floating body in incident waves (full wave–body interaction).

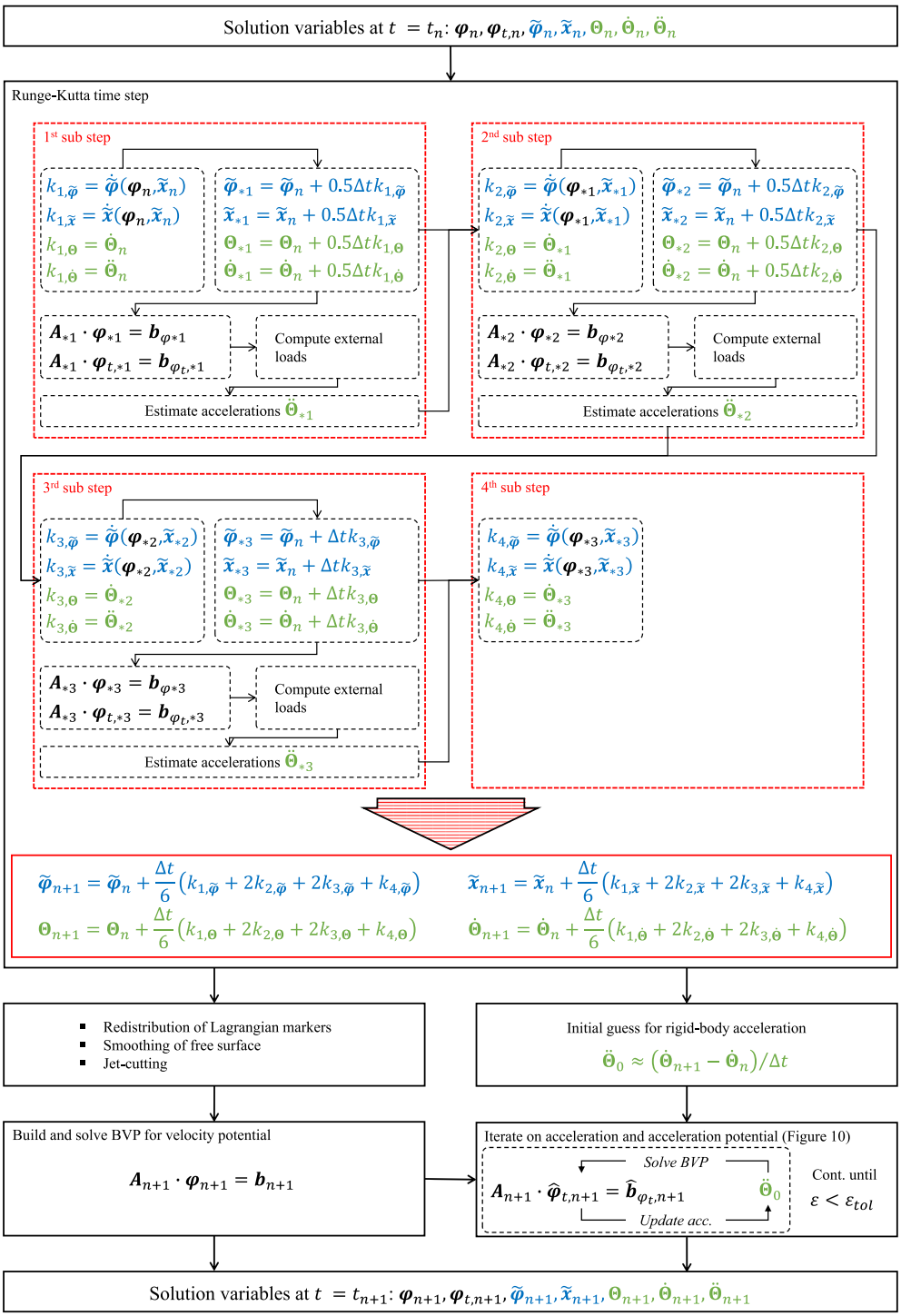

Fig. 13. Flowchart for one complete time step for a freely-floating body simulation. The black, blue and green symbols represent field, free-surface and rigid-body variables, respectively. $\ddot{\Theta}^0$ represent the estimated rigid-body accelerations that are updated using the iterative scheme in Fig. 10 until the convergence criterion is met. In each iteration loop a new right-hand side vector $\hat{\boldsymbol{b}}_{\varphi_{t,n+1}}$ is obtained and new field variables $\hat{\boldsymbol{\varphi}}_{t,n+1}$ are estimated by solving the BVP for the time derivative of φ. (For interpretation of the references to colour in this figure legend, the reader is referred to the web version of this article.)

4.1. Wave propagation

The solver's ability to propagate waves with different nonlinear features, such as steep waves in deep water, wave–wave interaction and solitary waves in shallow water and a focused, plunging wave was documented by Hanssen et al. (2018). An additional study, considering waves with steepness close to a breaking criterion, is presented here for completeness. The basis is the experiments performed by Baarholm (2001) with periodic, steep waves to study wave impacts on deck structures with low clearance to the still-water level. The experiments were carried out in a wave flume 13.5 m long, 0.6 m wide and with a water depth h equal to 1.0 m. The wave elevation was measured in a single wave probe that we here assume was located in the middle of the tank, although Baarholm states that the location of the wave probe sometimes was changed between cases. The three cases denoted d03_003, n30_004 and n30_008 in Baarholm (2001) with characteristics

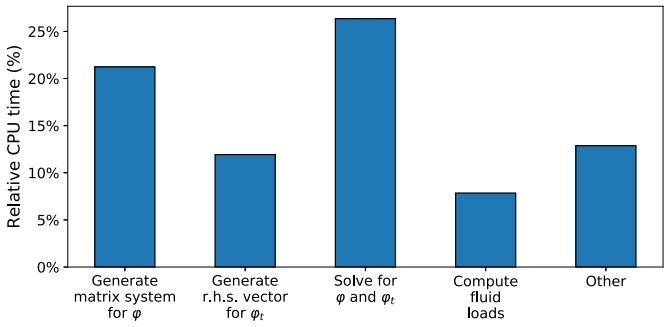

Fig. 14. Relative CPU time for main tasks in a simulation using the IBOGM with a freely floating body in the middle of the NWT.

Table 1
Selected periodic-wave cases from Baarholm (2001). ω is the angular wave frequency, λ is the wavelength, ζ_c is the crest amplitude, H_b is the breaking-wave height given by Eq. (36) and k is the wave number.

Case	ω (s^{-1})	λ (m)	ζ_c (m)	$0.5H_b$ (m)	$k\zeta_c$ (–)
d03_003	6.28	1.56	0.080	0.111	0.322
n30_004	6.28	1.56	0.093	0.111	0.375
n30_008	5.03	2.41	0.089	0.169	0.232

given in Table 1 are considered, where $k\zeta_c$ is a measure of the crest steepness. The table includes half the breaking-wave height H_b given by the following criterion in (Mei et al., 2005):

$$\frac{H_b}{\lambda} = 0.14 \tanh(kh). \tag{36}$$

This assumes that a wave breaks when the horizontal particle velocity in the crest exceeds the phase speed of the wave. Although ζ_c differs from $0.5H_b$ for nearly-breaking waves, the breaking-criterion indicates that especially the case n30_004 is close to wave breaking. The waves in the experiments were generated by a flap-type wavemaker hinged 0.1 m above the seabed. However, neither the stroke nor the ramp period of the wavemaker are known and have to be assumed. We here use a ramp time of 5 s, while the wavemaker's angular stroke $s_{wm,a}$ is approximated using linear wavemaker theory resulting in the following $s_{wm,a}$ values: 3.209° for d03_003, 3.638° for n30_004 and 4.498° for n03_008. The time step Δt and grid spacing $\Delta x = \Delta z$ are set to 0.02 s and 0.05 m, respectively, for all three cases. Similar grid spacings are used in the stationary background grid and in the body-fixed grid moving with the wavemaker. This gives at least 30 time steps per wave period and at least 31 grid points per wavelength. The length of the wave tank is increased to 16.5 m in the numerical analysis to allow for a 6 m long numerical beach with damping coefficient $\nu_{max} = 2.0\ s^{-1}$ at the opposite side of the wavemaker. The free-surface markers are semi-Lagrangian, i.e. only allowed to move in vertical direction.

The wave elevation in the probe located 6.25 m from the position of the wavemaker at rest is compared with the experimental results in Fig. 15 for the cases in Table 1. Given the uncertainty related to the wavemaker signal and the probe position used in the experiments, the agreement is deemed satisfactory. The largest deviations are observed for the case with ζ_c closest to $0.5H_b$ (n30_004), which may partly be explained by that modelling such steep wave is challenging both experimentally and numerically.

4.2. Forced heave motions of a semi-submerged circular cylinder in still water

The forced harmonic heave motion of a half-submerged, circular cylinder in still water studied experimentally by Tasai and Koterayama (1976) and numerically by Sun (2007) is considered. This case is characterized by two numerically challenging nonlinear features: (1)

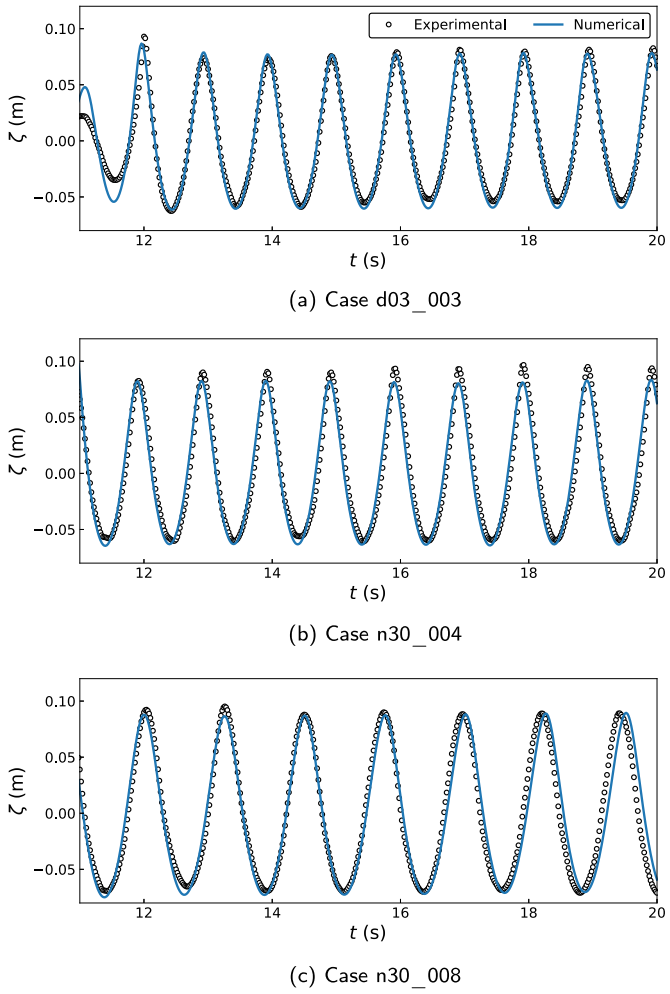

Fig. 15. Time series of wave elevation for the cases in Table 1 in a wave probe located 6.25 m from the position of the wavemaker. It is noted that B-spline interpolation is used to increase the spatial sampling density of the experimental results.

The body has non-vertical geometry where it intersects the free surface and (2) local nonlinear wave behaviour develops close to the body for high oscillation frequencies. It is noted that the main results for the heaving cylinder has already been documented in Hanssen et al. (2017). The cylinder has radius $R = 0.1$ m, and the heave motion is given as $\eta_3(t) = -\epsilon_{\eta_3} R \sin \omega t$ where $\epsilon_{\eta_3} = \eta_{3a}/R$ and ω are the non-dimensional heave amplitude and the angular oscillation frequency, respectively. From the time series of the vertical force $F_3(t)$ the heave added mass and damping coefficients, A_{33} and B_{33}, can be estimated as follows (Sun, 2007):

$$A_{33} = \frac{b_{3,1} - C_{33}\eta_{3a}}{-\omega^2 \eta_{3a}}, \tag{37}$$

$$B_{33} = \frac{a_{3,1}}{\omega \eta_{3a}}. \tag{38}$$

The hydrostatic restoring coefficient is defined as $C_{33} = \rho g D$ with ρ the water density, g the acceleration of gravity and $D = 2R$ the cylinder's diameter. The Fourier coefficients in Eqs. (37), (38) follow by expanding the heave-force signal in a Fourier series,

$$F_3(t) = F_{3,0} + \sum_{n=1}^{\infty} F_{3,n} \sin(n\omega t + \delta_n), \tag{39}$$

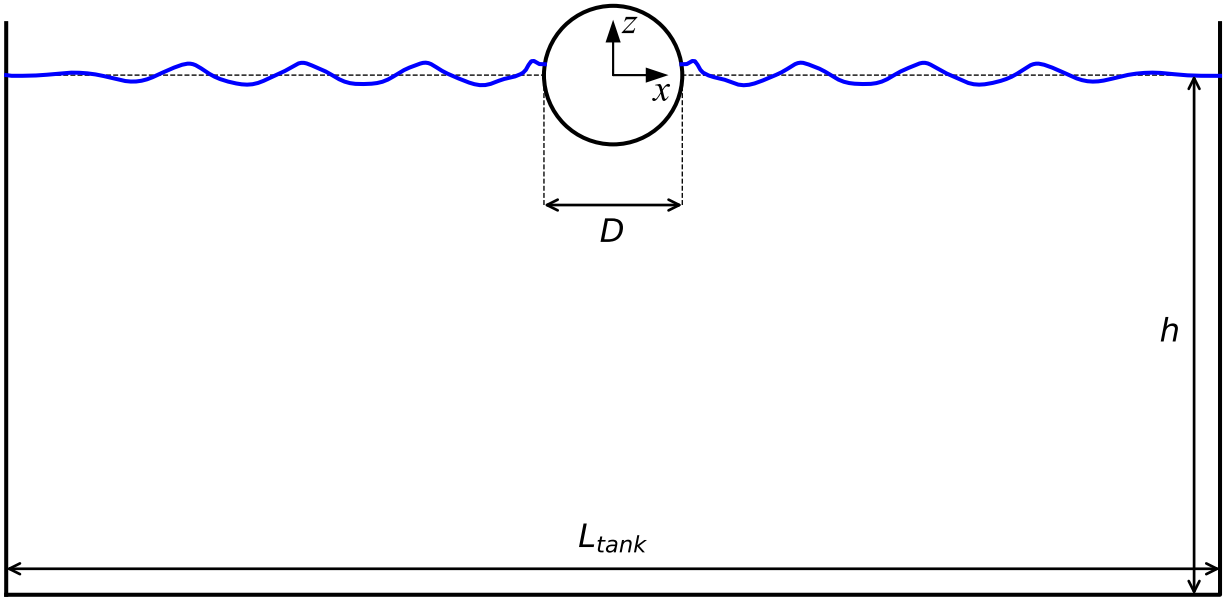

Fig. 16. Sketch of numerical wave tank used to analyse a heaving circular cylinder. L_{tank} and h is the tank length and water depth, respectively. The global Oxz coordinate system is located in the middle of the computational domain with origin in the still waterline.

where $F_{3,n}$ and δ_n are the nth order force amplitude and phase angle, respectively. The force amplitudes are estimated as

$$\begin{aligned} F_{3,0} &= \frac{1}{mT}\int_{t_0}^{t_0+mT} F_3(t)dt \equiv a_{3,0} \\ F_{3,n}\sin\delta_n &= \frac{2}{mT}\int_{t_0}^{t_0+mT} F_3(t)\cos(n\omega t)dt \equiv a_{3,n} \\ F_{3,n}\cos\delta_n &= \frac{2}{mT}\int_{t_0}^{t_0+mT} F_3(t)\sin(n\omega t)dt \equiv b_{3,n} \end{aligned} \qquad n \geq 1, \tag{40}$$

where $T = 2\pi/\omega$ is the oscillation period and $m \geq 1$ is the number of full oscillation periods used in the estimation taken so that $F_3(t)$ has steady-state behaviour for $t_0 \leq t < t_0 + mT$. The mean force $F_3^{(0)}$ and the second-order force amplitude $F_{3,2}$ are defined as

$$F_3^{(0)} = a_{3,0} - \rho g S_0 \tag{41}$$

and

$$F_{3,2} = \sqrt{a_{3,2}^2 + b_{3,2}^2}, \tag{42}$$

where $S_0 = 0.5\pi R^2$ is the mean submerged area of the cylinder.

Eight non-dimensional oscillation frequencies $0.20 \leq \omega^2 R/g \leq 1.61$ are analysed for a single heave amplitude $\epsilon_{\eta_3} = 0.2$. The computational domain is symmetric about the vertical axis through the cylinder centre (Fig. 16). The length of the numerical domain is $L_{tank} = 10\lambda$, where $0.39\ \text{m} \leq \lambda \leq 3.15\ \text{m}$ is the wavelength for the radiated waves estimated from the deep-water dispersion relation. The same water depth $h = 1.50$ m is used for all frequencies. Numerical beaches with length 2λ are used towards the tank walls on both sides of the cylinder to prevent wave reflections. The free surface is described using the hybrid formulation of the free-surface conditions (15) where the free-surface markers at the wave–body intersection points move in a fully-Lagrangian manner, and thus never separate from the body surface, while the markers in the background grid are semi-Lagrangian and thus restricted to move in parallel with the inertial z axis. The spacing between free-surface markers in the body-fixed grid is significantly smaller than in the stationary background grid, where the markers are distributed so that their horizontal positions coincide with those of the grid nodes. The dimension of the overlapping body-fixed grid, equal in both directions, is $20R$ for the lowest and $5R$ for the highest frequency. All grids are uniform with square cells, where the grid spacing in the background grid is taken as $\Delta x = \Delta z \approx \lambda/18$. In the body-fixed grid $\Delta x_{bf} = \Delta z_{bf}$ is taken between $R/9$ and $R/5$, where the former is required for the most challenging high-frequency cases and the latter is considered a minimum to give a proper description of the cylinder's geometry in the IBM. The time step is taken in the range $T/200 \leq \Delta t \leq T/55$, where the smallest time step was required for the highest frequency $\omega^2 R/g = 1.61$. For this frequency, large free-surface curvatures develop close to the wave–body intersection points so that the jet-cutting scheme is activated. The main simulation parameters are summarized in Table 2.

Table 2
Simulation parameters used in the numerical analysis of a semi-submerged circular cylinder undergoing forced heave motion. $\omega^2 R/g$ is the non-dimensional heave frequency, L_{bf} is the dimension of the square body-fixed grid, Δx and Δx_{bf} are the uniform grid spacings in the background grid and body-fixed grids, respectively, Δt is the time step and $T = 2\pi/\omega$ is the heave period.

$\omega^2 R/g$ (–)	L_{bf} (m)	Δx (m)	Δx_{bf} (m)	$T/\Delta t$ (–)
0.20	2.00	0.176	0.017	55
0.40	1.00	0.087	0.014	70
0.60	0.85	0.059	0.013	85
0.80	0.70	0.044	0.012	85
1.01	0.60	0.035	0.012	150
1.19	0.50	0.030	0.012	150
1.38	0.50	0.025	0.011	200
1.61	0.50	0.022	0.011	200

The added mass and damping coefficients and the mean and second-order forces derived with the present (IBOGM) method are compared with reference results from various sources in Fig. 17. The theoretical results for A_{33} and B_{33} are derived by Tasai and Koterayama (1976) with a linear theory, while the theoretical results for $F_3^{(0)}$ and $F_{3,2}$ are computed by Papanikolaou (1980) using a second-order theory. The experimental results are by Tasai and Koterayama (1976), while the results by Sun (2007) are obtained from a nonlinear boundary element method (BEM). All the reference results are extracted from plots in Sun (2007). The IBOGM results for A_{33}, B_{33} and $F_{3,2}$ are in good agreement with the references, and especially with the numerical results by Sun. For $F_3^{(0)}$, where it should be noted that there is some scatter in the experimental data and that the values are small, some differences can be observed.

The case with $\omega^2 R/g = 1.61$, found to be the most numerically challenging case due to large free-surface curvatures close to the cylinder,

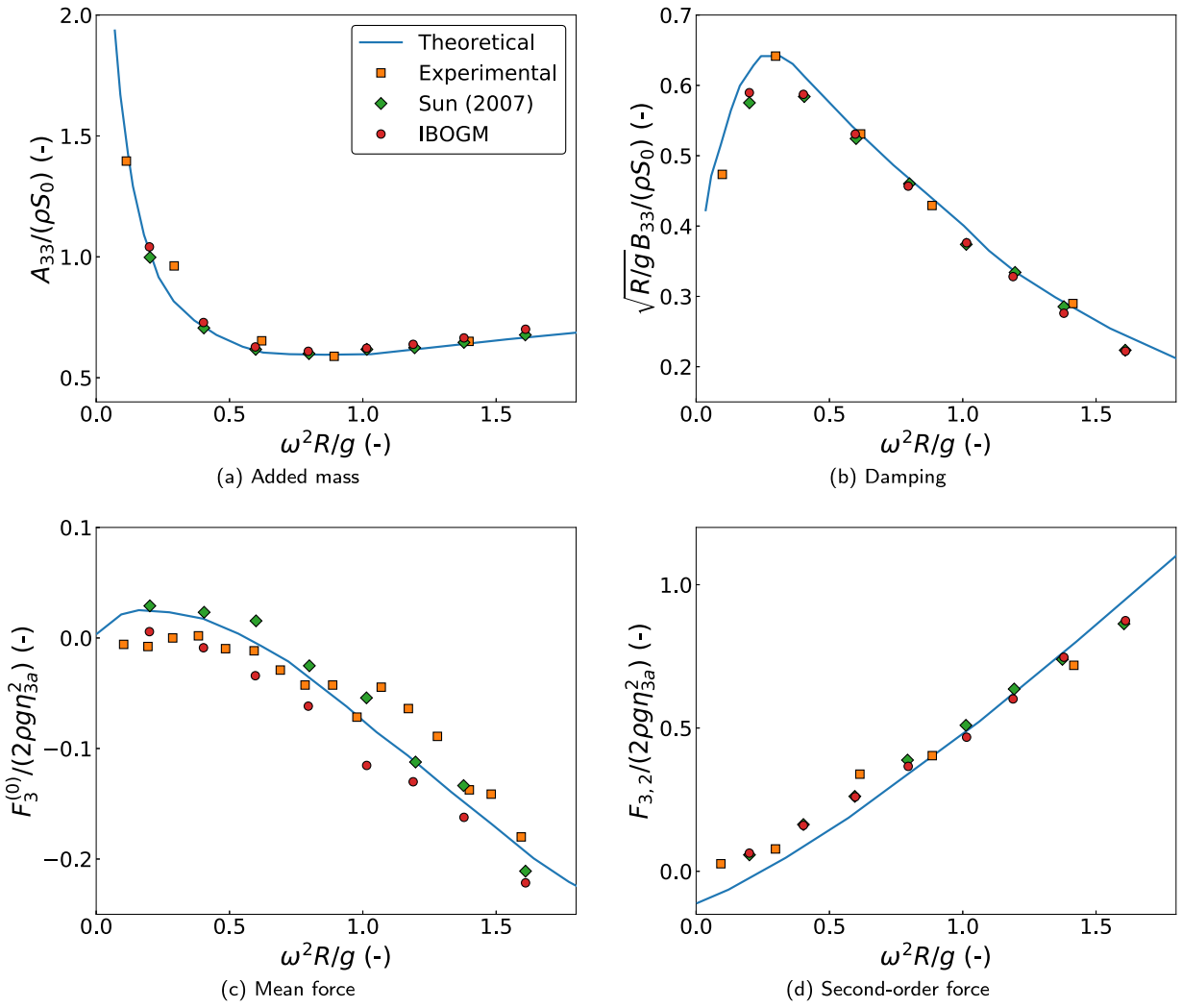

Fig. 17. Added mass and damping coefficients and mean and second-order forces in heave for cylinder undergoing forced heave motion with non-dimensional amplitude $\epsilon_{\eta_3} = 0.2$ and non-dimensional frequency $\omega^2 R/g$. All experimental results and the theoretical results for A_{33} and B_{33} are by Tasai and Koterayama (1976). The theoretical results for $F_3^{(0)}$ and $F_{3,2}$ are by Papanikolaou (1980). The results by Sun (2007) are computed by a nonlinear BEM.

is further examined. The time series of the heave force on the cylinder, containing higher-order harmonics, is compared with results from the analysis by Sun in Fig. 18. The two curves are generally consistent, and the differences observed in the troughs are considered acceptable, comparing two different methods for a numerically challenging case. The free-surface elevation close to the cylinder at six different time instants throughout an oscillation cycle for $\omega^2 R/g = 1.61$ is compared with Sun's results (obtained through personal communication) in Fig. 19. Consistent behaviour between the two solvers are observed both close to the wave–body intersection points and further away from the cylinder, indicating that the present numerical modelling of the flow at the wave–body intersection points is physically sound even with significant local nonlinear behaviour of the free surface.

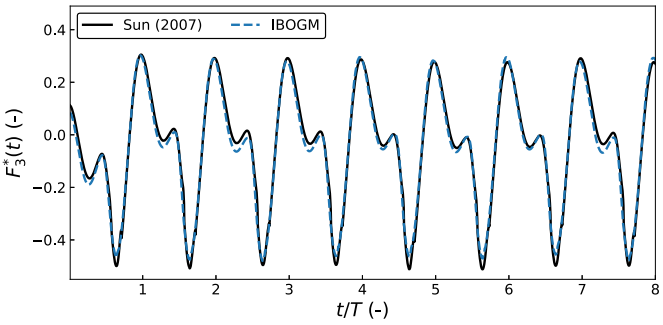

Fig. 18. Non-dimensional heave force $F_3^*(t) = (F_3(t) - \rho g S_0)/(2\rho g R \eta_{3a})$ for the case with $\epsilon_{\eta_3} = 0.2$, $\omega^2 R/g = 1.61$.

4.3. A fixed 2D ship section in regular waves

A 2D ship section in beam-sea regular waves was studied experimentally by Nojiri and Murayama (1975) (in Japanese) and later numerically by Tanizawa et al. (1999). The ship section has breadth $B = 0.50$ m, draught $h = 0.25$ m and bilge radius 0.064 m. Since the present analysis is performed in 2D, we define the fictitious length of the ship section in y direction as $L_s = 1.0$ m. The incident periodic waves are characterized by their non-dimensional wave frequency $\xi_B = \omega^2 B/2g = kB/2$ and a linear amplitude $\zeta_A = 0.5H$ with H the wave height. Here ω is the angular wave frequency, g is the acceleration of gravity and k is the wave number as given by the linear dispersion relation assuming deep-water conditions. The associated wavelength is $\lambda = 2\pi/k$. The waves included for the fixed ship section are defined in Table 3. All simulations are performed for $20T$ where $T = 2\pi/\omega$ is the wave period. A sketch of the numerical wave tank used in the analysis is shown in Fig. 20. The length of the tank L_{tank} is equal to

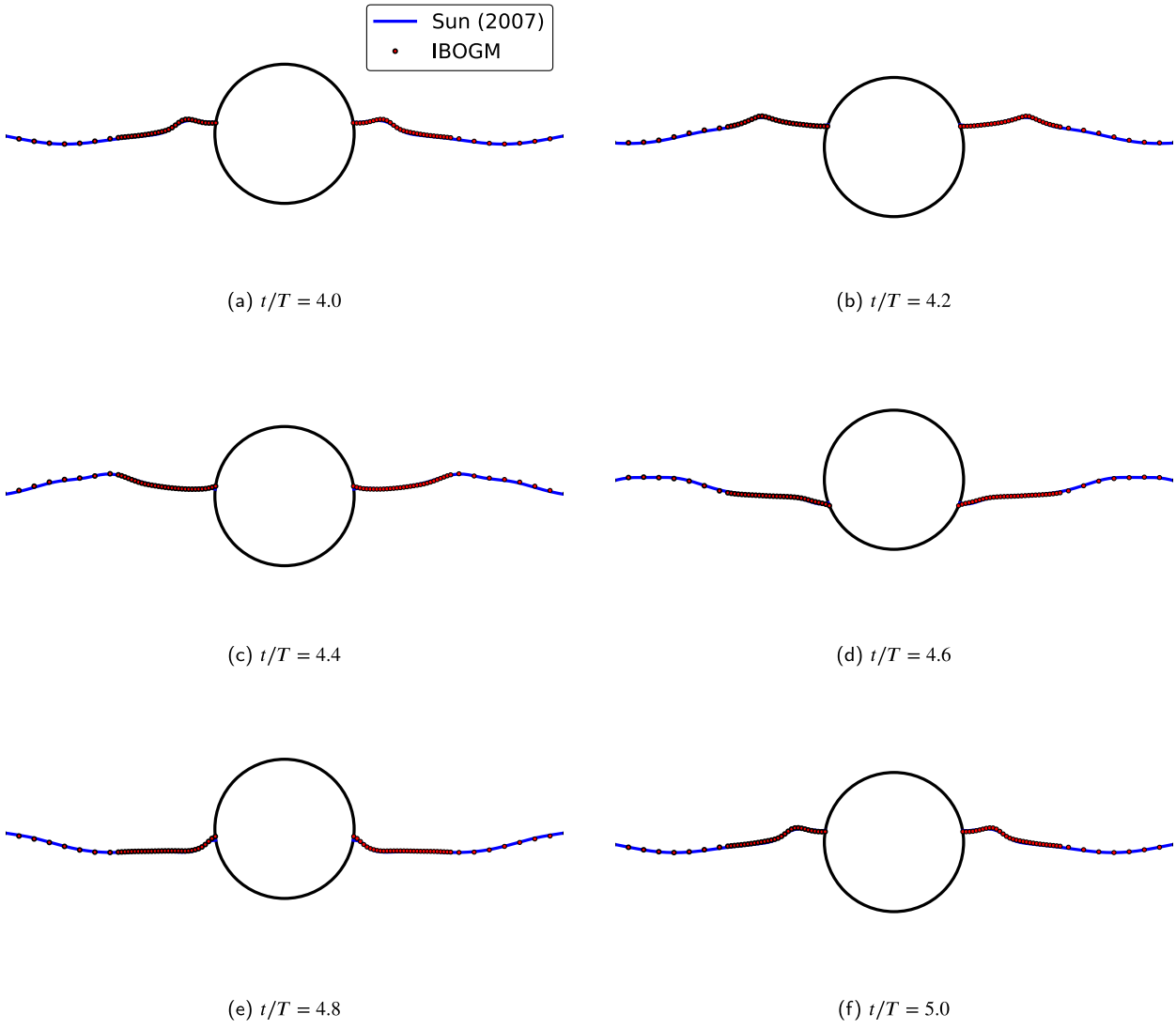

Fig. 19. Free-surface profile plotted at different time instants during one complete oscillation cycle with period T for the case with $\epsilon_{\eta_3} = 0.2$, $\omega^2 R/g = 1.61$.

8λ and the depth $h = \lambda$, i.e. deep-water conditions. The ship section is located in the middle of the tank with numerical beaches with length $L_{beach} = 2\lambda$ located on both sides. The beach on the wavemaker-side uses linear wavemaker theory as reference solution. The incident waves are generated with a rotating flap-type wavemaker hinged a distance $0.5h$ from the seabed. The wavemaker strokes required to obtain the waves specified in Table 3 are estimated using linear wavemaker theory (Dean and Dalrymple, 1991), and the duration of the ramp function is $4T$.

For all cases in Table 3, a time step $\Delta t = T/45$ is used. In the background grid and the body-fixed grid following the motion of the wavemaker, the uniform grid spacings are $\lambda/25$. In the square ship-section fixed grid, that has sides at least $2.5B$ long, the grid spacing is taken as the minimum between $B/12$ and $\lambda/25$. As an example, the grids used in the simulation with $\xi_B = 0.25$ are shown in Fig. 21. For this case, λ is much larger than B, hence the grid spacing in the ship section-fixed grid is much smaller than in the background grid.

Transfer functions for the mean wave-drift force in sway (x direction) and first-order wave loads in sway, heave and roll are presented in Fig. 22. The IBOGM results are compared to linear and experimental results by Nojiri and Murayama (1975) and nonlinear BEM results by Tanizawa et al. (1999). For the mean wave-drift force, the theoretical curve is derived by Nojiri and Murayama (1975) from a second-order theory. The mean wave-drift forces by Tanizawa et al. (1999) and in the IBOGM analyses are obtained from direct pressure integration (DPI). Several methods to estimate the mean wave-drift force have been systematically compared, where it is concluded that DPI is the most accurate. The details of this comparison, being outside the scope of the present paper, will be documented in a future publication.

Table 3
Definition of incident periodic waves. $\xi_B = \omega^2 B/2g$ and ω are the non-dimensional and dimensional wave frequencies, respectively, k is the wave number and $k\zeta_A$ is the wave steepness based on the linear wave amplitude ζ_A.

ξ_B (–)	k (m^{-1})	ω (s^{-1})	$k\zeta_{A,H=1cm}$ (–)	$k\zeta_{A,H=7cm}$ (–)
0.250	1.000	3.132	0.005	0.035
0.500	2.000	4.429	0.010	0.070
0.550	2.200	4.645	0.011	0.077
0.600	2.400	4.851	0.012	0.084
0.650	2.600	5.049	0.013	0.091
0.700	2.800	5.240	0.014	0.098
0.750	3.000	5.424	0.015	0.105
1.000	4.000	6.263	0.020	0.140
1.250	5.000	7.002	0.025	0.175
1.500	6.000	7.671	0.030	0.210
1.750	7.000	8.285	0.035	0.245
2.000	8.000	8.857	0.040	0.280

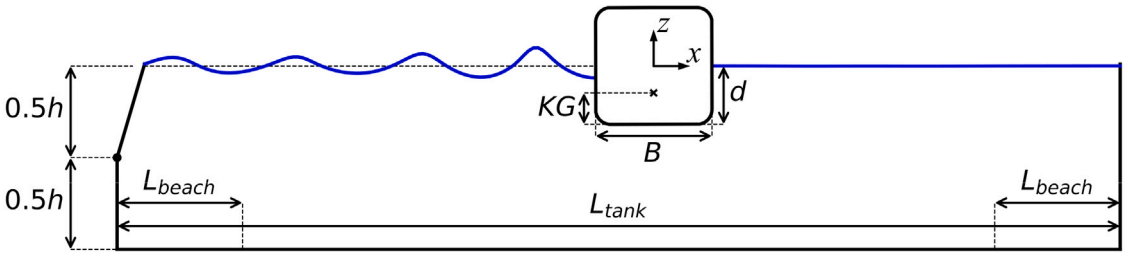

Fig. 20. Sketch of wave tank with length L_{tank} and water depth h. Waves are generated by a flap-type wavemaker hinged at half the water depth. Numerical damping zones with equal lengths $L_{beach} = 2\lambda$ are located at both ends of the tank. The global, Earth-fixed Oxz coordinate system is located in the middle of the computational domain with origin in the still waterline.

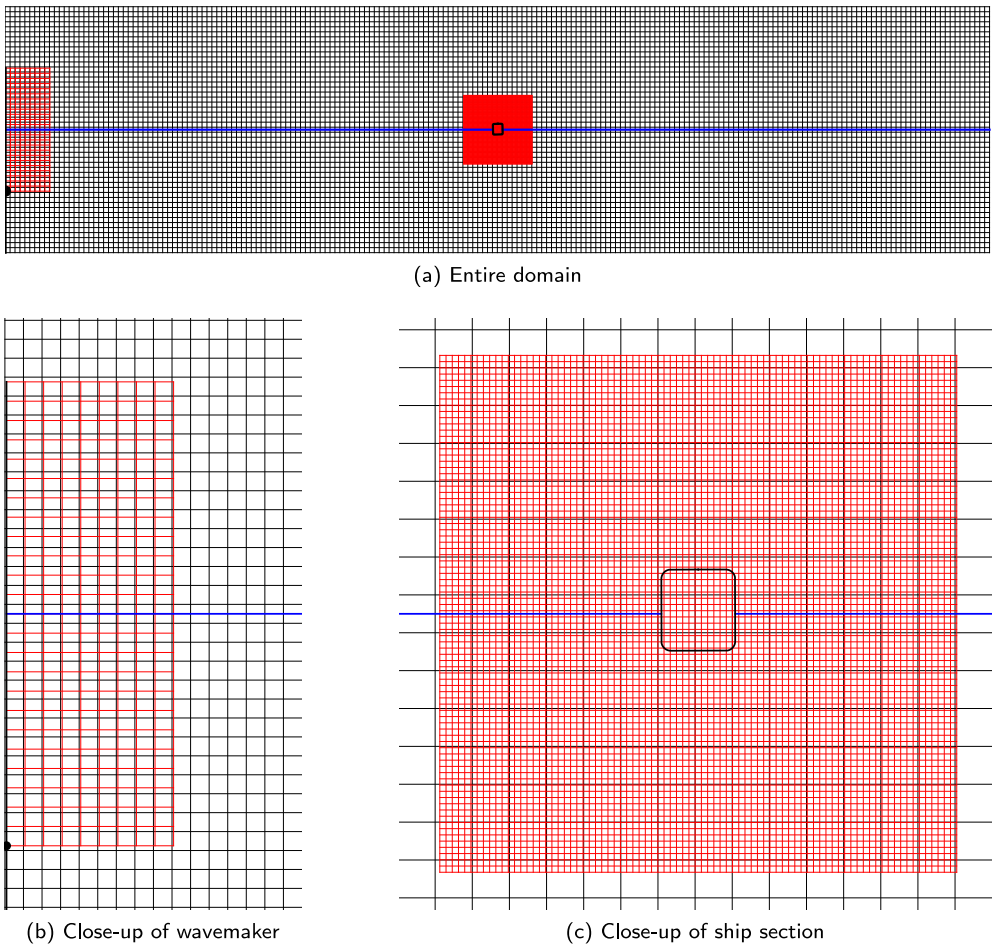

Fig. 21. Example of grids used for the case $\xi_B = 0.25$ shown at the initial time $t = 0$.

The IBOGM transfer functions are obtained from a Fourier analysis over the last four wave periods of the force time histories where steady-state behaviour is ensured. The wave height used in the experiments is not known. However, for the freely floating scenario, results for wave heights 3, 5 and 7 cm are presented. It is thus reasonable to assume that the experiments presented for the fixed body are performed with one of these. The first-order wave loads obtained with the IBOGM for both $H = 1$ cm and $H = 7$ cm are generally consistent with the reference results. For the largest wave frequencies, some scatter is seen in the experimental results which may be due to wave nonlinearity, experimental uncertainty or a combination of the two. The roll moments presented by Tanizawa et al. (1999) are consistently slightly larger than the linear, experimental and IBOGM values. The first-order wave loads show little sensitivity to the wave height. For the mean wave-drift force, the IBOGM results are consistent with the second-order theory up to $\xi_B = 1.0$, but give lower values above this frequency. The difference increases with increasing wave height, indicating higher-than-second-order effects. The same behaviour is qualitatively observed in the experimental results. Tanizawa et al. (1999) present larger mean wave-drift forces than the IBOGM for $\xi_B \geq 1.0$, but with the same qualitative ξ_B dependence. The reason for this difference is not fully understood, but the fact that Tanizawa et al. (1999) use a NWT with $L_{tank} = 6\lambda$ instead of 8λ (as used here) may contribute. Moreover, it is understood that Tanizawa et al. (1999) generate waves at a fixed control surface using linear wave theory instead of using a physical wavemaker, which may induce an artificial steady (Stokes-type) drift (Shao, 2010).

4.4. A freely floating 2D ship section in regular waves

The same 2D ship section as considered in the previous section is analysed here as freely floating for the largest wave height in Table 3.

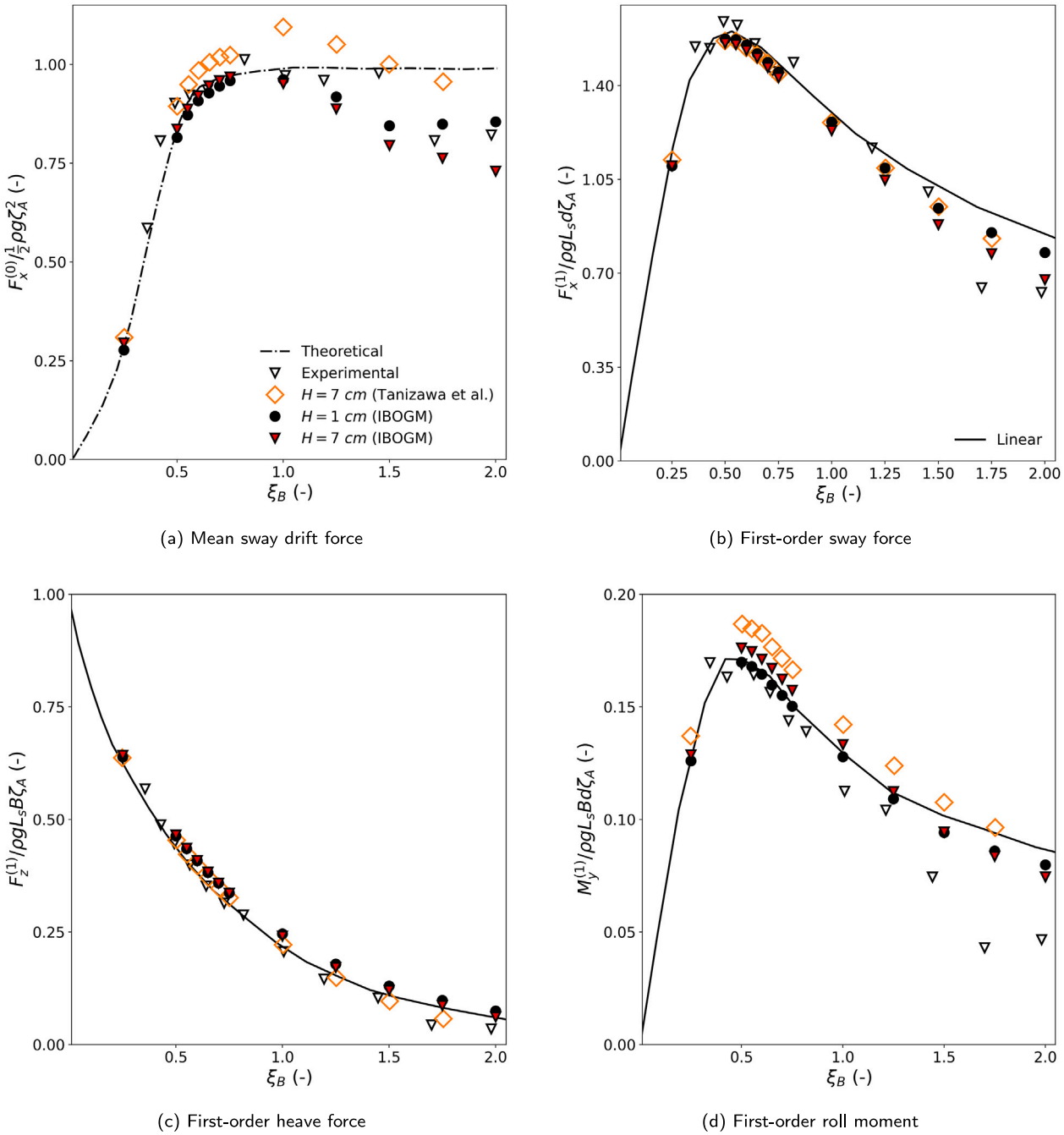

(a) Mean sway drift force

(b) First-order sway force

(c) First-order heave force

(d) First-order roll moment

Fig. 22. Transfer functions for mean sway wave-drift force and first-order wave loads on a fixed 2D ship section in beam-sea waves. IBOGM results compared with experimental, linear and second-order theoretical results by Nojiri and Murayama (1975) and nonlinear BEM results by Tanizawa et al. (1999).

The ship section has mass $M = 125$ kg, roll inertia $I_{yy} = 4.0145$ kg m^2 and the vertical centre of gravity is $KG = 0.135$ m from the keel. A linear sway damping $B^l_{22} = 19.8$ N s^{-1} and sway stiffness $C_{22} = 197.58$ N m^{-1}, acting in the body's centre of gravity, are included with the remaining damping and stiffness terms set to zero. All parameters are taken from Tanizawa et al. (1999). The damping and stiffness forces relate to motion in the inertial reference frame. The simulations length is $60T$, i.e. three times longer than for the fixed ship section. This is because transient motions are slowly decaying, so that it takes longer to reach approximately steady-state conditions. The duration of the wavemaker ramp function is also here $4T$. The time step and grid spacings are similar to those used for the fixed ship section. The IBOGM results are verified against analyses performed with the nonlinear potential-flow BEM solver developed by Greco (2001), using a NWT with identical dimensions and set-up as Fig. 20. Waves are generated with the same flap-type wavemaker, using identical wavemaker signals, and the damping and stiffness coefficients are the same as used in the present (IBOGM) analysis. Also the BEM solves an auxiliary BVP for the time derivative of φ. The main difference between the two simulations is that the time step in the BEM analyses is half of that in the IBOGM analyses, which was necessary in order to ensure numerical stability, and that the BVPs for φ and its time derivative are solved in an Earth-fixed reference frame in the BEM solver. The BEM analysis is therefore considered as an independent verification of the IBOGM analysis using a similar numerical set-up, but a fundamentally different numerical method.

Transfer functions for the mean wave-drift force in sway and first-order motions in sway, heave and roll are compared in Fig. 23. The

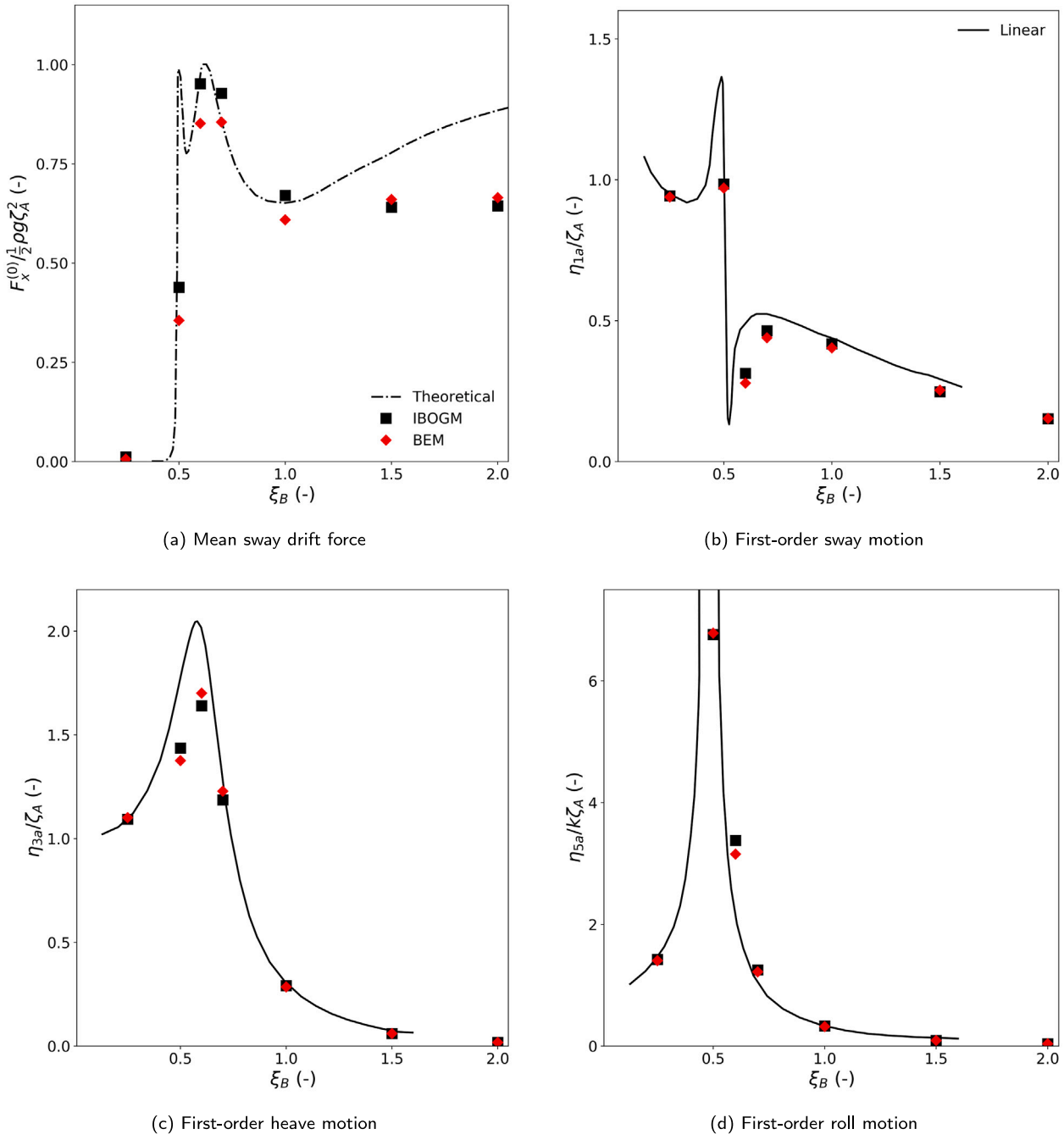

(a) Mean sway drift force

(b) First-order sway motion

(c) First-order heave motion

(d) First-order roll motion

Fig. 23. Transfer functions for mean sway wave-drift force and first-order motions compared with BEM results by Greco and linear results by Koo and Kim (2004). Theoretical values for the mean wave-drift force are taken from the same reference. The mean wave-drift forces from the IBOGM and BEM analyses are estimated using DPI.

IBOGM and BEM transfer functions are obtained from an identical Fourier analysis of the last $10T$ of the simulation time series. The plots include motions from a linear analysis by Koo and Kim (2004), and mean wave-drift force from a second-order theory by the same authors. Away from the heave and roll resonance frequencies around $\xi_B = 0.5$, both solvers produce motions in good agreement with the linear results. Significant differences from linear results are observed moving towards resonance frequencies, indicating non-negligible nonlinear effects. With roll amplitudes of approximately 30° close to resonance, the simulations are numerically challenging, and the consistency between the two nonlinear numerical methods are therefore encouraging. The mean wave-drift force in both the IBOGM and BEM analyses deviate from the theoretical curve for the steepest waves, which is consistent with the behaviour for the fixed ship section in Fig. 22. Close to the resonance-frequency region, the IBOGM gives slightly larger drift forces than the BEM. Since the mean wave-drift force is sensitive to the relative motion between the structure and waves, it is suggested that this may be related to the slight difference in heave motions observed in the frequency range $0.5 \leq \xi_B \leq 0.7$. The reason for these differences are not further explored, but it should be noted that the heave and roll motions are large, and the motions and loads in the different degrees of freedom are coupled with each other.

The IBOGM and BEM analyses for the challenging case with $\xi_B = 0.5$ can be further examined by comparing motion and load time series in Fig. 24, showing that the roll moments and motions are visually in excellent agreement. Consistent with the transfer functions in Fig. 23, the IBOGM gives slightly larger heave amplitudes, while the sway

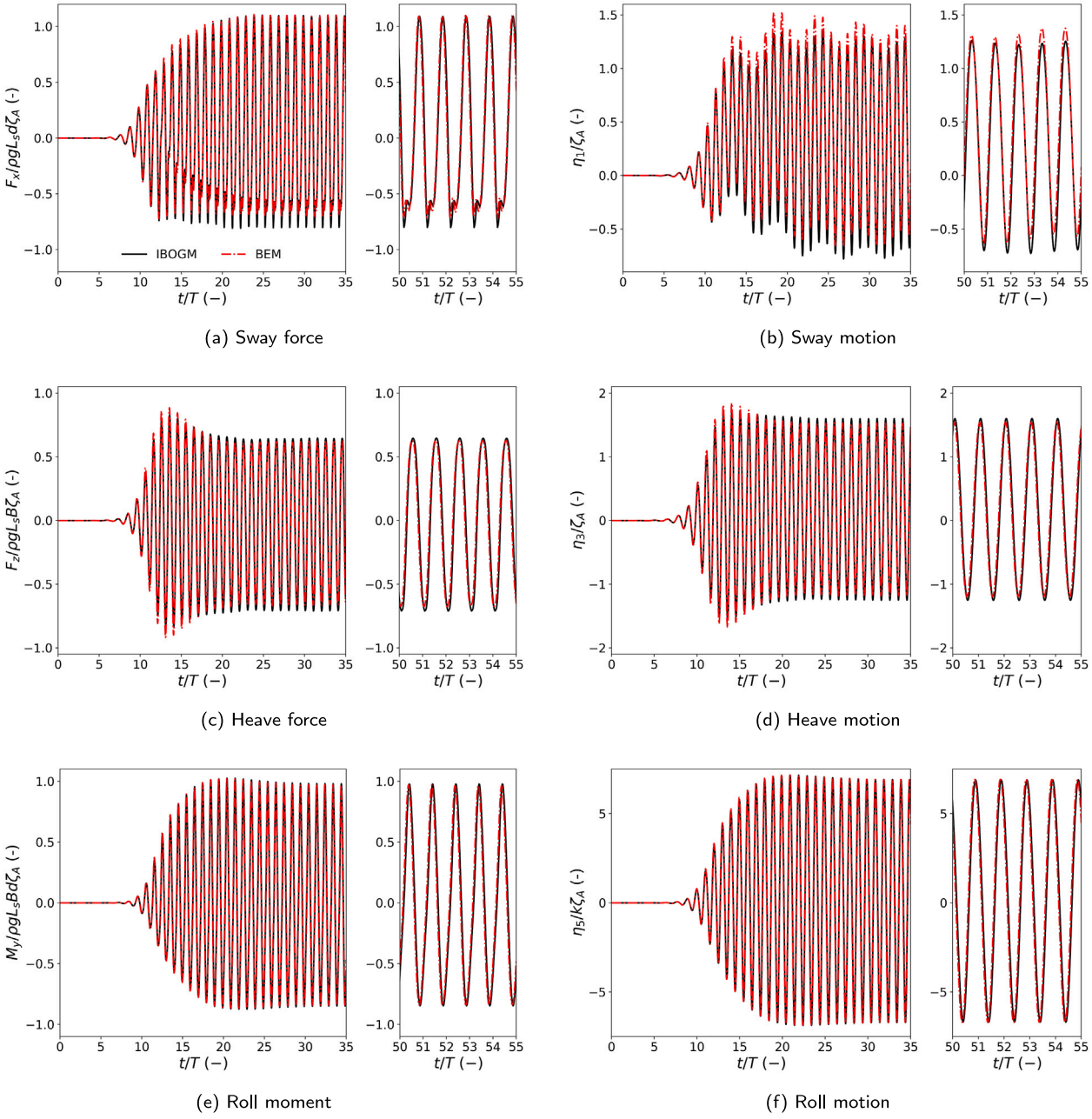

Fig. 24. Time series of wave loads and rigid-body motions compared with BEM results by Greco for $\xi_B = 0.5$, $H = 7$ cm.

forces differ mainly in the troughs. Although not easy to observe, the average sway force over the ten last wave periods (i.e. the mean wave-drift force) is slightly larger for the IBOGM than for the BEM. A Fourier analysis shows that these differences are mainly of third order. To finalize the verification, Fig. 25 shows an analysis of the wave elevation close to the ship section, and the dynamic-pressure distribution over the instantaneous wetted surface, for ten different time instants towards the end of the simulations. The time series of the sway force is included in each sub plot, with the exact time instant of the snapshot indicated. One should note that, because there is a slight difference in when data are written to file in the IBOGM and BEM analyses, the two simulations are not fully synchronized in all of the sub plots. However, for sub plots (b), (g) and (i), where the time instants approximately coincide, the results are in good agreement. Although there are local differences in the pressure distribution and the wave elevation, the instantaneous positions of the ship section and the sway forces are similar. One should keep in mind that these snapshots are taken towards the end of the simulations for a challenging case with roll motions up to 30°, where one may anticipate that inconsistencies between the two solvers would have escalated. The fact that the two distinctly different solvers give consistent results strengthens the confidence in the IBOGM.

5. Conclusions

A numerical wave tank (NWT) for nonlinear wave and wave-rigid body interactions in 2D using potential-flow theory has been presented. The modelling techniques are developed with future extension to 3D in mind. The harmonic polynomial cell (HPC) method, which is a higher-order accurate and efficient field method using overlapping cells, is employed to solve the Laplace equations for the velocity potential and its time derivative. An immersed boundary method (IBM) is proposed to model the free surface and body boundaries and is combined with using overlapping grids following the motion of rigid bodies. The combined method, representing a novel extension to the HPC method, was

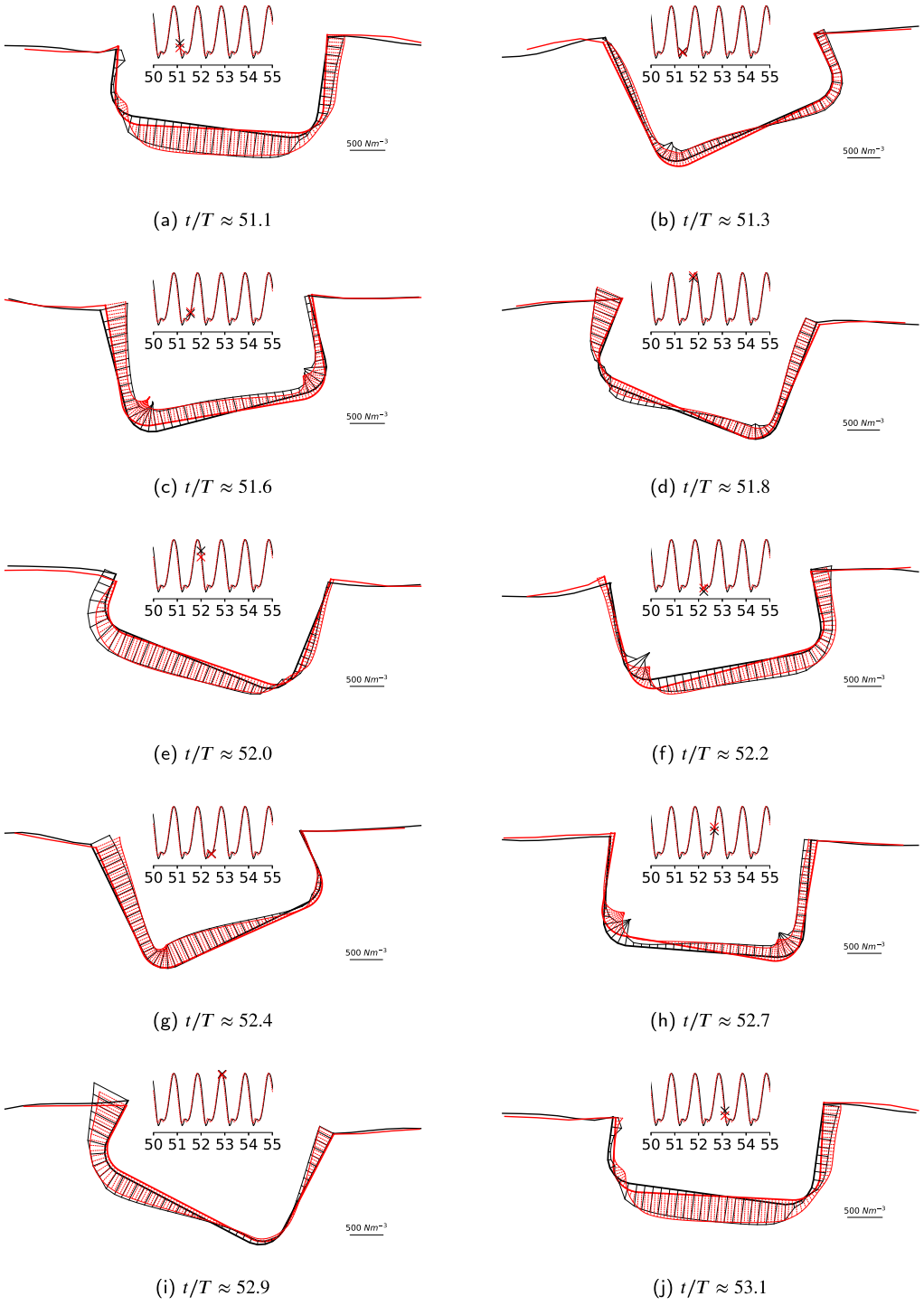

Fig. 25. Dynamic pressure distribution and free-surface elevation at different time instances for $\xi_B = 0.5$, $H = 7$ cm for IBOGM analysis (black) and Greco's BEM analysis (red). The corresponding time instants in the sway-force time series are indicated. (For interpretation of the references to colour in this figure legend, the reader is referred to the web version of this article.)

denoted as an immersed boundary-overlapping grid method (IBOGM). A consequence of using immersed boundaries is that we operate with ghost nodes and ghost cells, where a numerical solution exists in the part of the ghost cells outside the water region. The solution in these regions has no physical meaning. The IBOGM has the following main advantages: (1) Boundary-fitted grids, that may be cumbersome to generate for complex boundaries and that must be updated every time the boundaries move, are avoided. (2) Cartesian grids with square cells can be used throughout, which is important to maximize the accuracy in the HPC method. (3) The solution may be refined locally by increasing the density of overlapping grids without increasing the number of unknowns unnecessarily.

The following validation and verification cases were presented: (1) Propagation of regular waves with steepness up to the theoretical breaking limit, (2) forced harmonic heave motion of a semi-submerged circular cylinder in still water, and a 2D ship section with a small bilge radius (3) fixed and (4) freely floating in beam-sea regular waves. (1)–(3) consider wave propagation, wave radiation and wave diffraction separately, whereas in (4) all effects are combined. The results from the present analysis agreed well with experimental, theoretical and

numerical reference results. In particular, for the freely floating 2D ship section, results were systematically compared with a dedicated independent analysis performed with a fully nonlinear boundary element method (BEM) code. The comparison included challenging scenarios with resonant roll motions up to 30°. The two analyses gave generally consistent loads and motions, both indicating significant nonlinear coupling effects near heave and roll resonance. Both analyses gave mean sway wave-drift forces smaller than second-order theory for steep waves. Close to heave and roll resonance, slightly different wave-drift forces were observed between the two analyses. However, the differences were considered acceptable, since the wave-drift forces are sensitive to the first-order motions that were large in this frequency range.

The cases presented in this paper indicate that the proposed IBOGM method handles wave and wave-rigid body interaction effects accurately. It is therefore considered well-suited for further examination of nonlinear wave–body interaction effects.

CRediT authorship contribution statement

Finn-Christian Wickmann Hanssen: Developing and implementing numerical method, Numerical analysis, Preparing paper. **Marilena Greco:** Supervision, Discussing results, Independent BEM analysis.

Declaration of competing interest

The authors declare that they have no known competing financial interests or personal relationships that could have appeared to influence the work reported in this paper.

Acknowledgements

This work has been carried out at the Centre for Autonomous Marine Operations and Systems (AMOS). The Research Council of Norway (Norges Forskningsråd) is acknowledged as the main sponsor of AMOS, Norway. This work was supported by the Research Council of Norway through the Centre of Excellence funding scheme, Project number 223254-AMOS.

References

Baarholm, R.J., 2001. Theoretical and Experimental Studies of Wave Impact Underneath Decks of Offshore Platforms (Ph.D. thesis). Norwegian University of Science and Technology.

Bardazzi, A., Lugni, C., Antuono, M., Graziani, G., Faltinsen, O.M., 2015. Generalized hpc method for the Poisson equation. J. Comput. Phys. 299, 630–648.

Bingham, H.B., Zhang, H., 2007. On the accuracy of finite-difference solutions for nonlinear water waves. J. Eng. Math. 58 (1–4), 211–228.

Dean, R.G., Dalrymple, R.A., 1991. Water Wave Mechanics for Engineers and Scientists. World Scientific Publishing Company.

Dommermuth, D.G., Yue, D.K., Lin, W., Rapp, R., Chan, E., Melville, W., 1988. Deep-water plunging breakers: A comparison between potential theory and experiments. J. Fluid Mech. 189, 423–442.

Ducrozet, G., Bingham, H.B., Engsig-Karup, A.P., Ferrant, P., 2010. High-order finite difference solution for 3d nonlinear wave-structure interaction. J. Hydrodyn. Ser. B 22 (5), 225–230.

Eatock Taylor, R., 1996. Analysis of non-linear wave-body interactions using finite elements. In: Waves and Nonlinear Processes in Hydrodynamics. Springer, pp. 51–62.

Engsig-Karup, A.P., Bingham, H.B., Lindberg, O., 2009. An efficient flexible-order model for 3d nonlinear water waves. J. Comput. Phys. 228 (6), 2100–2118.

Faltinsen, O.M., 1993. Sea Loads on Ships and Offshore Structures. Cambridge university press.

Faltinsen, O.M., Timokha, A.N., 2009. Sloshing. Cambridge University Press Cambridge.

Fonseca, N., Ommani, B., Stansberg, C., Bøckmann, A., Birknes-Berg, J., Nestegård, A., Hauteclocque, G.d., Baarholm, R., 2017. Wave forces and low frequency drift motions in extreme seas: Benchmark studies. In: Offshore Technology Conference.

Fonseca, N., Stansberg, C.T., 2017a. Wave drift forces and low frequency damping on the exwave fpso. In: ASME 2017 36th International Conference on Ocean, Offshore and Arctic Engineering. American Society of Mechanical Engineers.

Fonseca, N., Stansberg, C.T., 2017b. Wave drift forces and low frequency damping on the exwave semi-submersible. In: ASME 2017 36th International Conference on Ocean, Offshore and Arctic Engineering. American Society of Mechanical Engineers.

Fonseca, N., Stansberg, C.T., Nestegård, A., Bøckmann, A., Baarholm, R., 2016. The EXWAVE JIP: Improved procedures to calculate slowly varying wave drift forces on floating units in extreme seas. In: ASME 2016 35th International Conference on Ocean, Offshore and Arctic Engineering. American Society of Mechanical Engineers.

Fredriksen, A.G., 2015. A Numerical and Experimental Study of a Two-Dimensional Body with Moonpool in Waves and Current (Ph.D. thesis). Norwegian University of Science and Technology.

Greco, M., 2001. A Two-Dimensional Study of Green-Water Loading (Ph.D. thesis). Norwegian University of Science and Technology.

Hanssen, F.-C.W., 2019. Non-Linear Wave-Body Interaction in Severe Waves (Ph.D. thesis). Norwegian University of Science and Technology.

Hanssen, F.-C.W., Bardazzi, A., Lugni, C., Greco, M., 2018. Free-surface tracking in 2D with the harmonic polynomial cell method: Two alternative strategies. Internat. J. Numer. Methods Engrg. 113 (2), 311–351.

Hanssen, F.-C.W., Colicchio, G., Greco, M., 2019. Severe wave-body interactions: A potential-flow hpc method and its strong domain-decomposition coupling with a level-set Navier-Stokes solver. In: The 34th International Workshop on Water Waves and Floating Bodies.

Hanssen, F.-C.W., Greco, M., Faltinsen, O.M., 2017. Wave-body interaction with overlapping structured grids in the hpc method. In: The 32nd International Workshop on Water Waves and Floating Bodies.

Hanssen, F.-C.W., Greco, M., Shao, Y.-L., 2015. The harmonic polynomial cell method for moving bodies immersed in a cartesian background grid. In: ASME 2015 34th International Conference on Ocean, Offshore and Arctic Engineering. American Society of Mechanical Engineers.

de Hauteclocque, G., Rezende, F., Waals, O., Chen, X.-B., 2012. Review of approximations to evaluate second-order low-frequency load. In: ASME 2012 31st International Conference on Ocean, Offshore and Arctic Engineering, Vol. 44885. American Society of Mechanical Engineers, pp. 363–371.

Kim, C., Clement, A., Tanizawa, K., 1999. Recent research and development of numerical wave tanks - a review. Int. J. Offshore Polar Eng. 9 (04).

Koo, W., Kim, M.-H., 2004. Freely floating-body simulation by a 2D fully nonlinear numerical wave tank. Ocean Eng. 31 (16), 2011–2046.

Kvitrud, A., 2014a. Anchor line failures - norwegian continental shelf - 2010-2014. Report, Petroleum Safety Authority Norway.

Kvitrud, A., 2014b. Lessons learned from Norwegian mooring line failures 2010–2013. In: ASME 2014 33rd International Conference on Ocean, Offshore and Arctic Engineering. American Society of Mechanical Engineers.

Liang, H., Faltinsen, O.M., Shao, Y.-L., 2015. Application of a 2D harmonic polynomial cell (hpc) method to singular flows and lifting problems. Appl. Ocean Res. 53, 75–90.

Liang, H., Santo, H., Shao, Y.-L., Law, Y.Z., Chan, E.S., 2020. Liquid sloshing in an upright circular tank under periodic and transient excitations. Phys. Rev. Fluids 5 (8), 084801.

Ma, S., Hanssen, F.-C.W., Siddiqui, M.A., Greco, M., Faltinsen, O.M., 2018. Local and global properties of the harmonic polynomial cell method: In-depth analysis in two dimensions. Internat. J. Numer. Methods Engrg. 113 (4), 681–718.

Ma, Q., Yan, S., 2009. Qale-fem for numerical modelling of non-linear interaction between 3d moored floating bodies and steep waves. Internat. J. Numer. Methods Engrg. 78 (6), 713–756.

Mei, C.C., Stiassnie, M., Yue, D.K.-P., 2005. Theory and Applications of Ocean Surface Waves: Nonlinear Aspects. World scientific.

Noble Denton Europe, 2006. Floating Production System JIP FPS Mooring Integrity. Technical Report, Research report 444 prepared for the Health and Safety Executive (HSE).

Nojiri, N., Murayama, K., 1975. A study on the drift force on two-dimensional floating body in regular waves (in Japanese). Trans. West-Japan Soc. Nav. Archit. 51, 131–152.

Papanikolaou, A., 1980. Second-order theory of oscillating cylinders in a regular steep wave. In: Proc. 13th Symp. on Nav. Hydrodyn., pp. 303–331.

Patterson, B.D., Mo, F., Borgschulte, A., Hillestad, M., Joos, F., Kristiansen, T., Sunde, S., Van Bokhoven, J.A., 2019. Renewable co2 recycling and synthetic fuel production in a marine environment. Proc. Natl. Acad. Sci. 116 (25), 12212–12219.

Robaux, F., Benoit, M., 2018. Modeling nonlinear wave-body interaction with the harmonic polynomial cell method combined with the immersed boundary method on a fixed grid. In: The 33rd International Workshop on Water Waves and Floating Bodies.

Robaux, F., Benoit, M., 2020. Development and validation of a numerical wave tank based on the harmonic polynomial cell and immersed boundary methods to model nonlinear wave-structure interaction. arXiv preprint arXiv:2009.08937.

Savitzky, A., Golay, M.J., 1964. Smoothing and differentiation of data by simplified least squares procedures. Anal. Chem. 36 (8), 1627–1639.

Shao, Y.-L., 2010. Numerical Potential-Flow Studies on Weakly-Nonlinear Wave-Body Interactions with/without Small Forward Speeds (Ph.D. thesis). Norwegian University of Science and Technology.

Shao, Y.-L., Faltinsen, O.M., 2012. Towards efficient fully-nonlinear potential-flow solvers in marine hydrodynamics. In: Proceedings of the 31st International Conference on Ocean, Offshore and Arctic Engineering (OMAE), Rio de Janeiro, Brazil. American Society of Mechanical Engineers, pp. 369–380.

Shao, Y.-L., Faltinsen, O.M., 2014a. Fully-nonlinear wave-current-body interaction analysis by a harmonic polynomial cell method. J. Offshore Mech. Arct. Eng. 136, 031301.

Shao, Y.-L., Faltinsen, O.M., 2014b. A harmonic polynomial cell (hpc) method for 3d Laplace equation with application in marine hydrodynamics. J. Comput. Phys. 274, 312–332.

Shen, Y., Greco, M., Faltinsen, O.M., Ma, S., 2020. Numerical study towards closed fish farms in waves using two harmonic polynomial cell methods. In: The 35th International Workshop on Water Waves and Floating Bodies.

Siddiqui, M.A., Greco, M., Colicchio, G., Faltinsen, O.M., 2018. Validation of damaged ship hydrodynamics by a domain decomposition approach using the harmonic polynomial cell method and openfoam. In: The 33rd International Workshop on Water Waves and Floating Bodies.

Strand, I.M., 2018. Sea Loads on Closed Flexible Fish Cages (Ph.D. thesis). Norwegian University of Science and Technology.

Sun, H., 2007. A Boundary Element Method Applied to Strongly Nonlinear Wave-Body Interaction Problems (Ph.D. thesis). Norwegian University of Science and Technology.

Tanizawa, K., 1995. A nonlinear simulation method of 3d body motions in waves. J. Soc. Nav. Archit. Jpn. 178, 96–105.

Tanizawa, K., Minami, M., Naito, S., 1999. Estimation of wave drift force by numerical wave tank. In: The Ninth International Offshore and Polar Engineering Conference. International Society of Offshore and Polar Engineers.

Tasai, F., Koterayama, W., 1976. Nonlinear hydrodynamic forces acting on cylinders heaving on the surface of a fluid. Technical Report, Research Institute for Applied Mechanics, Kyushu University, Fukuaka, Japan.

Tong, C., Shao, Y.-L., Bingham, H.B., Hanssen, F.-C.W., 2021. An adaptive harmonic polynomial cell method with immersed boundaries: Accuracy, stability and applications. Internat. J. Numer. Methods Engrg. http://dx.doi.org/10.1002/nme.6648, (in press).

Vinje, T., Brevig, P., 1981. Breaking Waves on Finite Water Depths: A Numerical Study. Ship Research Institute of Norway Marine Technology Center.

Wang, J., Faltinsen, O.M., Duan, W.Y., 2020. A high-order harmonic polynomial method for solving the Laplace equation with complex boundaries and its application to free-surface flows. part i: Two-dimensional cases. Internat. J. Numer. Methods Engrg. 121 (17), 3893–3925.

Wu, G., Eatock Taylor, R., 1994. Finite element analysis of two-dimensional non-linear transient water waves. Appl. Ocean Res. 16 (6), 363–372.

Xu, Y., Bingham, H.B., Shao, Y.-L., 2020. Finite difference solutions for nonlinear water waves using an immersed boundary method. Internat. J. Numer. Methods Fluids.

Yan, S., Ma, Q., 2007. Numerical simulation of fully nonlinear interaction between steep waves and 2d floating bodies using the qale-fem method. J. Comput. Phys. 221 (2), 666–692.

You, J., 2012. Numerical Studies on Wave Forces and Moored Ship Motions in Intermediate and Shallow Water (Ph.D. thesis). Norwegian University of Science and Technology.

Zhu, W., Greco, M., Shao, Y.-L., 2017. Improved hpc method for nonlinear wave tank. Int. J. Nav. Archit. Ocean Eng. 9 (6), 598–612.